Ice Nucleation Parameterization and Relative Humidity Distribution in Idealized Squall-Line Simulations

MINGHUI DIAO

Department of Meteorology and Climate Science, San Jose State University, San Jose, California

GEORGE H. BRYAN, HUGH MORRISON, AND JORGEN B. JENSEN

National Center for Atmospheric Research,[a] *Boulder, Colorado*

(Manuscript received 8 December 2016, in final form 5 June 2017)

ABSTRACT

Output from idealized simulations of a squall line are compared with in situ aircraft-based observations from the Deep Convective Clouds and Chemistry campaign. Relative humidity distributions around convection are compared between 1-Hz aircraft observations (≈250-m horizontal scale) and simulations using a double-moment bulk microphysics scheme at three horizontal grid spacings: $\Delta x = 0.25$, 1, and 4 km. The comparisons focus on the horizontal extent of ice supersaturated regions (ISSRs), the maximum and average relative humidity with respect to ice (RHi) in ISSRs, and the ice microphysical properties during cirrus cloud evolution, with simulations at 0.25 and 1 km providing better results than the 4-km simulation. Within the ISSRs, all the simulations represent the dominant contributions of water vapor horizontal heterogeneities to ISSR formation on average, but with larger variabilities in such contributions than the observations. The best results are produced by a $\Delta x = 0.25$-km simulation with the RHi threshold for initiating ice nucleation increased to 130%, which improves almost all the ISSR characteristics and allows for larger magnitude and frequency of ice supersaturation (ISS) > 8%. This simulation also allows more occurrences of clear-sky ISSRs and a higher spatial fraction of ISS for in-cloud conditions, which are consistent with the observations. These improvements are not reproduced by modifying other ice microphysical processes, such as a factor-of-2 reduction in the ice nuclei concentration; a factor-of-10 reduction in the vapor deposition rate; turning off heterogeneous contact and immersion freezing; or turning off homogeneous freezing of liquid water.

1. Introduction

Numerical simulations of mesoscale convective systems (MCS) have been a very useful tool for analyzing the structure and evolution of squall lines, examining theories about squall-line development and maintenance, and conducting model sensitivity tests based on various initial conditions, boundary conditions, and model setups (Bryan et al. 2006; Hane 1973; Thorpe et al. 1982; Fovell and Ogura 1989; Fovell and Dailey 1995; Robe and Emanuel 2001; Parker and Johnson 2004; James et al. 2005; Szeto and Cho 1994). Cloud-resolving model (CRM) simulations can explicitly resolve motions with scales of 1–10 km depending on the selected horizontal resolution, and, with increasing supercomputing power, they can provide a detailed, three-dimensional representation of convective systems as well as their thermodynamic and microphysical processes (e.g., Bryan 2012; Bryan and Morrison 2012; Bryan and Parker 2010; Trier et al. 2006; Bryan and Rotunno 2009a,b; Bryan 2005; Bryan and Rotunno 2007; Stern et al. 2016; Rotunno et al. 2016).

Previous studies have shown that many simulated properties of squall lines (e.g., structure, morphology, and rainfall rate) are subject to influences from various grid resolutions and cloud microphysics parameters (Bryan et al. 2006; Bryan and Morrison 2012; Xu et al. 2002; Bryan et al. 2003). Increasing the horizontal grid spacing from 1 to 12 km, Weisman et al. (1997) showed

[a] The National Center for Atmospheric Research is sponsored by the National Science Foundation.

Corresponding author: Minghui Diao, minghui.diao@sjsu.edu

Publisher's Note: This article was revised on 6 June 2019 to include a funder acknowledgement in the Acknowledgements section that was omitted when originally published.

DOI: 10.1175/JAS-D-16-0356.1

that significantly higher precipitation amounts by ~20%–30% were produced in the upshear region of the gust front using the larger spacing. The influences of liquid- and ice-phase microphysical processes on simulations of MCS have also been investigated. Morrison et al. (2009) showed that by allowing the intercept parameter N_0 of the gamma size distribution for cloud and precipitation particles to evolve with the prognosed number and mass mixing ratios in a two-moment (2-M) microphysics scheme, the simulated trailing stratiform precipitation region became more extensive with a reduced rain evaporation rate, while the convective region showed increasing rain evaporation rates and weaker convective cells. The inclusion of ice species, as well as the detailed treatment of ice microphysical properties, can also largely affect the structure and development of simulated squall lines (e.g., Fovell and Tan 1998; McCumber et al. 1991; Ferrier et al. 1995). Fundamentally, the inclusion of ice species (e.g., cloud ice, snow, and graupel) adds a new source and sink of latent heat and thereby can affect the thermodynamic and dynamical structure of simulated convective systems (e.g., Adlerman and Droegemeier 2002; Johnson et al. 1993; Straka and Anderson 1993). Liu et al. (1997) reported that when simulating tropical squall lines with weak environmental convective instability in a CRM, both the maximum vertical velocity and the total precipitation intensity increase when ice microphysics is included based on the bulk parameterization of Koenig and Murray (1976). Comparing simulated and observed squall lines, Bryan and Morrison (2012) showed that the inclusion of graupel as the rimed species in a 2-M microphysics scheme produces different rainfall amount and cold pool intensities than inclusion of hail. In addition, their simulation using the 2-M scheme with hail at the finest horizontal grid spacing examined (i.e., 0.25 km) produces the most similar distributions of reflectivity and cold pool properties compared with observations.

A crucial condition associated with ice microphysical processes is ice supersaturation (ISS). ISS is the prerequisite condition for ice crystal formation, and it occurs when relative humidity with respect to ice (RHi) is greater than 100%. ISS has been frequently observed by in situ observations in both clear-sky and in-cloud conditions, in the tropical tropopause layer and extratropical upper troposphere and lower stratosphere (UT/LS) (Diao et al. 2014a; Jensen et al. 2001; Heymsfield et al. 1998; Ovarlez et al. 2002; Krämer et al. 2009). The formation and evolution of ice crystals are tightly correlated with the background relative humidity. Homogeneous nucleation of submicron aerosols is largely determined by the conditions of ISS and temperature, and the nucleation rate of ice is positively correlated with the magnitudes of ISS after certain ISS thresholds have been reached (Pruppacher and Klett 2010). For heterogeneous nucleation, the number of ice nuclei (IN) activated below water saturation is also related to the magnitudes of ISS (Phillips et al. 2013). Furthermore, the vapor depositional growth rate of a single ice particle is correlated with the ambient ISS (Rogers and Yau 1989). Because of the relationships between relative humidity and ice microphysical processes, it is critical to examine the characteristics of ISS as part of the evaluation of ice microphysical processes in the CRMs.

Several characteristics of ISS that affect the subsequent formation and evolution of ice crystals include the magnitude and frequency of ISS, the spatial extent and patchiness of ISS regions (ISSRs), and their coexistence with ice crystals. In observational studies, the frequency distributions of ISS with respect to various temperatures have been used as an indicator for identifying the occurrences of different mechanisms for ice particle formation (i.e., homogeneous and heterogeneous freezing) (Cziczo et al. 2013). Based on a pole-to-pole flight campaign (Diao et al. 2014a), ~54% and ~46% of the in-cloud conditions at $T \leq -40°C$ were found to coexist with ISS and non-ISS conditions, respectively, indicating that ISS conditions frequently intersect with cirrus clouds or reside within them. The coexistence of ISS and ice crystals is challenging to represent in simulations since it is affected by interactions of multiple microphysical processes, including ice nucleation, freezing of cloud droplets or rain drops, vapor deposition, aggregation, and sedimentation. However, neglecting or oversimplifying this transition can lead to significant impacts on the atmospheric radiative transfer budget. For example, representing the observed ISS incorrectly as ice particles in cirrus clouds in a radiative transfer model leads to an average increase of ~3–4 $W m^{-2}$ in the top of the atmosphere net radiation flux (Tan et al. 2016). In addition, ISSRs that have a contiguous region of RHi greater than 100% are found to have large spatial heterogeneities with a median horizontal length of ~1 km, and ~97% of them collocate with large water vapor spatial heterogeneities (Diao et al. 2014a). The spatial relationship between ISSRs and ice crystals also was derived in an evolutionary view for in situ formed cirrus clouds (Diao et al. 2013b). Yet it is still unclear if these observed characteristics of ISS can be well represented in CRM simulations at various horizontal grid spacings.

Intercomparisons between CRMs and aircraft observations provide a unique tool to evaluate model performance. One caution is that certain characteristics of the simulations are case dependent, which leads to different or even contradictory comparison results among various case studies. In an intercomparison study among 10

CRMs, about one order of magnitude of differences was found in the simulated cloud water mixing ratio and from one to two orders of magnitude of differences in the ice mixing ratio (Xu et al. 2002). The authors commented that more model sensitivity tests would help to quantify the extent of model–observation differences, especially under the influences of various horizontal/vertical grid spacings and cloud microphysics parameterizations.

In this work, in situ observations from an aircraft campaign focused on convective activity over the continental United States are compared with idealized simulations of a squall line in a CRM. Statistical distributions of the characteristics of ISSRs derived from a composite observation dataset containing 22 flights are used to evaluate the model representation of ISSRs. Simulations with various horizontal grid spacings are conducted in the model–observation comparisons, and sensitivity tests on the representations of ISS and ice microphysical properties are provided. Section 2 describes the dataset and methodology in this comparison study, including the in situ airborne observations, the setup of the numerical simulations, and the experimental designs. Section 3 discusses the comparison results on ISSR characteristics between the observations and various model runs. Comparisons of the evolution of the average RHi, ice water content (IWC), and ice crystal number concentration (Nc) for in-cloud segments around convective activity are shown in section 4. Discussions on the analyses and implications for model development are given in section 5.

2. Dataset and methodology

a. *In situ aircraft observations and instrumentations in the DC3 flight campaign*

Airborne in situ measurements were obtained onboard the National Science Foundation (NSF)/National Center for Atmospheric Research (NCAR) Gulfstream-V (GV) research aircraft during the NSF Deep Convective Clouds and Chemistry (DC3) campaign from 18 May to 30 June 2012 (Barth et al. 2015). The DC3 campaign targeted deep convective systems in the southern United States, with research domains focusing on three regions: Alabama, Colorado, and Oklahoma–Texas. Here we use a composite dataset based on a total of 22 research flights onboard the GV aircraft to conduct a statistical analysis on the characteristics of ISSRs. Using a composite dataset provides a relatively large sample size, which helps to ensure that the statistical distributions of the ISSR characteristics and ice microphysical properties are representative for regions around the anvils and convective clouds. In addition, to quantify the differences between convective and nonconvective regions, the ISSR characteristics in the DC3 campaign are compared with a previous study on the NSF High-Performance Instrumented Airborne Platform for Environmental Research (HIAPER) Pole-to-Pole Observations (HIPPO) global campaign that mostly sampled in situ formed cirrus clouds (Diao et al. 2014a).

The key variables used in the analysis include measurements of water vapor, temperature, and ice crystals. Water vapor data were reported at 1-Hz resolution (i.e., ≈250-m horizontal scale) by the vertical cavity surface emitting laser (VCSEL) hygrometer. The VCSEL hygrometer is an open-path, 25-Hz, near-infrared laser hygrometer with ~6% accuracy and ≤1% precision (Zondlo et al. 2010). The VCSEL water vapor measurements have been used to analyze the characteristics of ISSRs and to validate remote sensing observations in several previous studies (Diao et al. 2013a, 2015, 2014a,b). The Rosemount temperature probe on the GV aircraft provides 1-Hz temperature measurements with uncertainties of ±0.3 K. When considering both the uncertainties from water vapor and temperature measurements, the uncertainties in RHi at the sample range of 207.4–233.15 K in the DC3 dataset are ~7.4%–6.9%, respectively.

The fast two-dimensional cloud (Fast-2DC) probe measures ice particles, and we use data accumulated at 1-Hz resolution, with a size range of 25–1600 μm. In this study, only particles greater than the detection limit of the third diode of the Fast-2DC probe (i.e., greater than 67.5 μm) are analyzed. Smaller particles are not considered in the analysis in order to minimize the potential impacts of ice shattering and other optical noise/interference. Similar to the previous analyses of in-cloud and clear-sky conditions based on the Fast-2DC probe measurements (Diao et al. 2014a, 2015), we define in-cloud conditions as occurring when the 1-Hz observations contain one or more ice particles in the 1-s measurements, which typically have $\mathrm{Nc} > 0.03\,\mathrm{L}^{-1}$ and $\mathrm{IWC} > 4 \times 10^{-5}\,\mathrm{g\,m}^{-3}$, and the remaining regions are defined as clear-sky conditions. We note that the sampling rate of the Fast-2DC is size dependent: for example, a single particle of 100 μm (1 mm) is sampled at approximately 10 (~33) $\mathrm{L\,s}^{-1}$.

b. *Numerical model setup and experimental design*

We use a three-dimensional nonhydrostatic numerical model [Cloud Model 1 (CM1)] for idealized simulations of a squall line (Bryan and Morrison 2012; Bryan and Parker 2010) with the double-moment microphysics scheme based on Morrison et al. (2005). This setup uses periodic lateral boundary conditions in the along-line direction (y direction), and open boundary conditions in the longer across-line (x) direction. The horizontal domain size is 576 km × 128 km with a duration of 10 h for

all the simulations. A total of 88 vertical levels are uniformly distributed with a grid spacing of $\Delta z = 250$ m, from the surface to 22 km. Three different horizontal grid spacings (Δx) are examined in this study: 0.25, 1, and 4 km (except for one special $\Delta x = 0.125$-km simulation with $\Delta t = 0.5$ s, discussed below). Because the vertical grid is the same for all simulations, we use the same time step ($\Delta t = 1$ s) for all simulations. The small vertical grid spacing ($\Delta z = 250$ m) ensures that 3D turbulence is produced for simulations at $\Delta x = 0.25$ km. We choose 250 m as the minimum horizontal grid spacing, since it is comparable to the ≈250-m horizontal resolution of the in situ sampling onboard the GV research aircraft at 1-Hz scale. The initial sounding profile as well as other configuration details follow Bryan and Morrison (2012), including using a Rayleigh damper for wave damping in the stratosphere and a cold pool condition (Weisman et al. 1997) to initialize the squall line. In addition, consistent with the simulations of Bryan and Morrison (2012), we neglect radiative transfer, surface heat fluxes, and Coriolis acceleration for simplicity and to maintain the same environment for all the simulations.

The comparisons between the observations and simulations are restricted to temperature ≤ -40°C, to ensure that no supercooled liquid water exists in our analysis of ISSRs and ice crystals. At this temperature range, ice crystals are formed in these simulations when RHi exceeds a threshold (108% by default) via a prognostic equation from Cooper (1986) as a function of temperature: $N_{ice} = 0.005 \times \exp[0.304 \times (273.15 - T)]$, where N_{ice} is ice crystal number concentration (L^{-1}) and T is temperature (K). The RHi > 108% threshold in the Cooper parameterization is a simplified parameter for initiating ice nucleation, since the homogeneous freezing thresholds derived from the laboratory results are dependent on various factors, such as temperature, aerosol size, and water activity (Koop et al. 2000). A threshold of Nc > 0.03 L^{-1} and IWC > 4×10^{-5} g m^{-3} (i.e., the minimum concentration and IWC of all ice hydrometers, including cloud ice, snow, and graupel) is used to define in-cloud conditions in the simulations, which is comparable to the threshold used in the observations. Note that observations have a limited sampling range of ice crystals, but this cannot account for the differences in Nc and IWC distributions in the results section. Examples of the CM1 simulations at 0.25, 1, and 4 km are shown in vertical and horizontal cross sections (Figs. 1, 2), illustrating patchier distributions of ISSRs in the 250-m simulations than the 1- and 4-km simulations. To be consistent with the RHi calculation in the observations, the RHi values in the simulations are derived from specific humidity based on the same equation used for the observations (Murphy and Koop 2005). Note that such calculation of RHi is slightly different by up to 0.34% from the RHi calculated based on Flatau et al. (1992) in the Morrison microphysics scheme.

c. *Mock aircraft sampling method*

We use "mock" aircraft flights within the simulations to sample conditions in space and time along a 1D trajectory, which mimics the sampling strategy of the real research aircraft. Specifically, we translate the locations of an arbitrary number of hypothetical airplanes and interpolate model conditions (temperature, water vapor mixing ratio, saturation vapor pressure, etc.) to these locations every model time step. All of the mock aircraft sample at a specified isobaric surface with a given translation speed along a prescribed direction. Here we set the mock aircraft speed at 250 m s^{-1} with one second sampling (except for a $\Delta x = 0.125$-km simulation with the mock aircraft speed of 125 m s^{-1}), which are comparable to the true airspeed of the GV research aircraft in the UT/LS (≈250 m s^{-1}). We note that the resolution of these mock aircraft data is 250 m for all the simulations at $\Delta x \geq 0.25$ km, even for the $\Delta x = 1$- and 4-km simulations, because we interpolate conditions to the mock aircraft positions, which can be located between grid points.

Since this work aims at statistical comparisons between the observations and simulations, we sample various conditions in the model simulations by using a total of 451 mock aircraft inserted at 451 isobaric levels, separated by 1-hPa increments between 150 and 600 hPa. These mock aircraft tracks provide a composite dataset composed of 1D horizontal transects at various isobaric levels, which are more continuous in time compared with the default model output at every 15 min. All the following comparisons between the observations and simulations are based on the composite DC3 observations of 22 fights and the composite simulations dataset of 451 mock aircraft for a duration of 10 h. Sensitivity tests of the mock aircraft sampling directions are also conducted by using three mock aircraft sampling directions: x (across-line), y (along-line), and diagonal (45° clockwise from the cross-line direction), which are here named as run-X, run-Y and run-Dia, respectively (Table 1).

d. *Defining five evolutionary phases of ice clouds*

The airborne in situ observations provide fast and accurate measurements yet only grasp an instantaneous "snapshot" of the atmosphere. Previously, a method has been applied to the 1D, aircraft-based observations in order to obtain a quasi-evolutionary view of the in situ observed cirrus clouds (Diao et al. 2013b, 2014b). Using this method, the evolutionary trend of ice microphysical properties inside cirrus clouds is derived, including the average RHi, Nc, and the mean diameter of ice crystals.

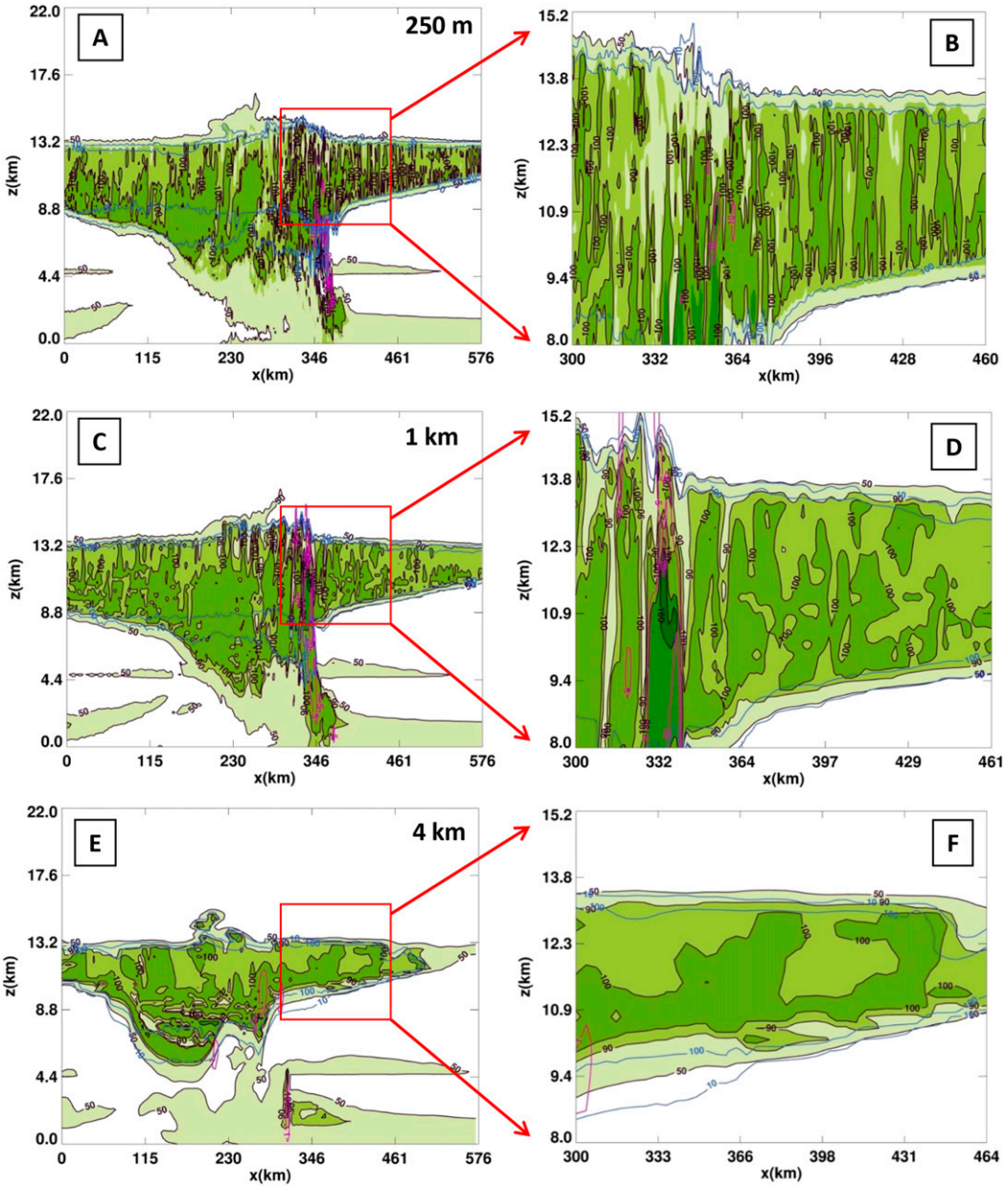

FIG. 1. Examples of vertical cross sections along the center of the idealized squall-line simulations at 6 h after the initialization. (a),(b) 250-m; (c),(d) 1-km; and (e),(f) 4-km horizontal grid spacings. Green shades and black lines denote the RH contours of 50%, 90%, and 100%. RHi is used for $T \leq 0°C$, and RH with respect to liquid is used for $T > 0°C$ based on the equations from Murphy and Koop (2005). Blue contours denote the Nc values (L^{-1}) at 10 and 100 L^{-1}. The purple contours denote vertical velocity at 10, 5, and 1 m s^{-1} in the 0.25-, 1-, and 4-km simulations, respectively.

In the work described herein, we extend the application of this method to compare the in situ observations with the mock aircraft sampling in simulations on the spatial relationship between ISSRs and ice crystal regions (ICRs: i.e., horizontal segments with continuous sampling of ice crystals). Five evolution phases are defined as: 1) ISSRs in clear-sky conditions (clear-sky ISSR phase), 2) ISSRs containing small ICRs (nucleation phase), 3) intersections between ISSRs and ICRs (early growth phase), 4) larger ICRs containing smaller ISSRs as a result of continuous depletion of vapor over ice saturation (later growth phase), and 5) ICRs with non-ISS conditions (sedimentation/sublimation phase) where all the vapor over ice saturation eventually has been depleted. Details for the definitions of these five evolution phases are explained in the previous study (Diao et al. 2013b).

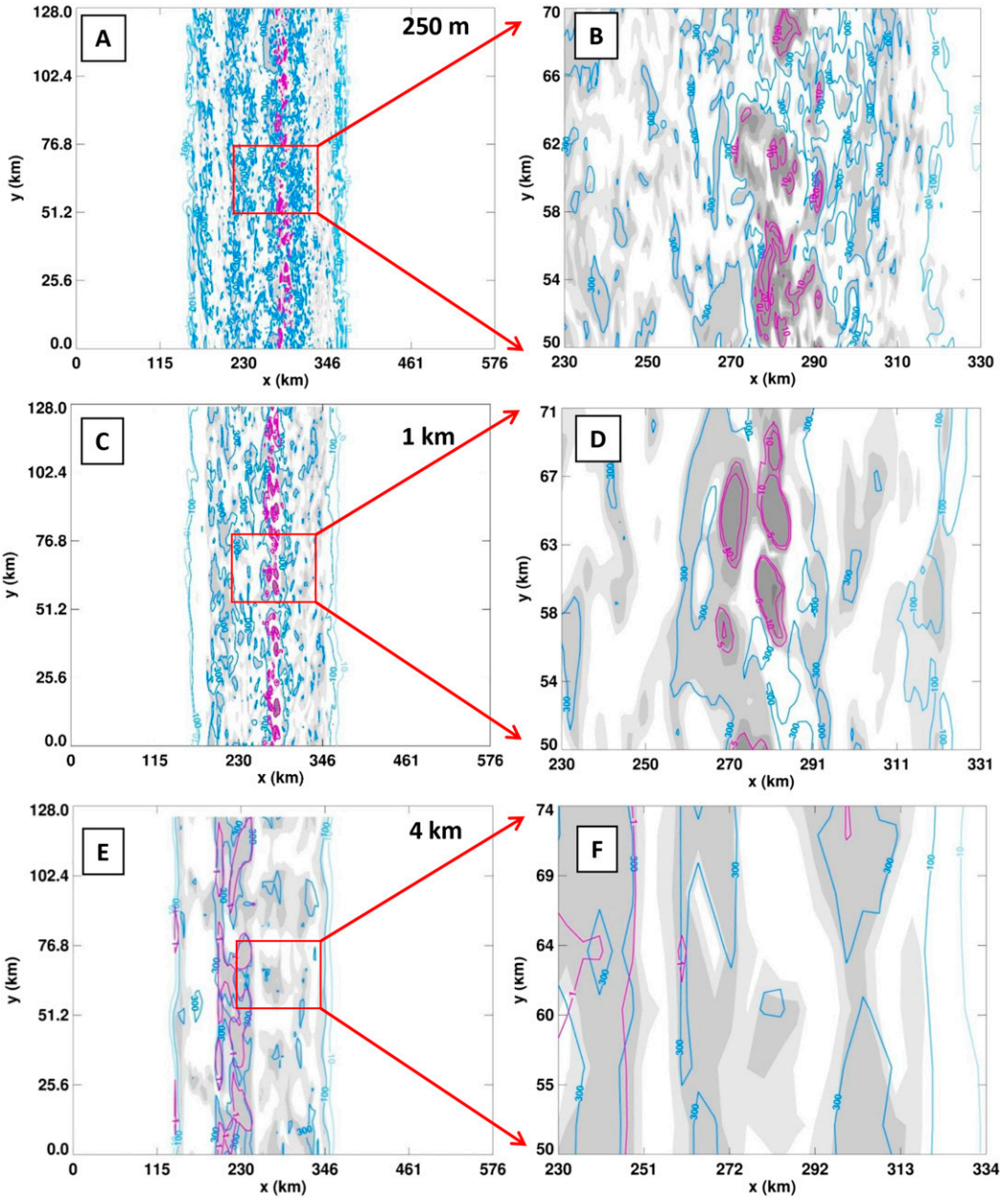

FIG. 2. Examples of horizontal cross sections at 10 km for the simulations at 6 h: (a),(b) 250 m; (c),(d) 1 km; and (e),(f) 4 km. Blue contours represent Nc at 10, 100, and 300 L^{-1}. Purple contours show vertical velocity at 10, 5, and 1 m s^{-1} in the 0.25-, 1-, and 4-km simulations, respectively. Gray shading from lighter to darker denotes RHi at 100%, 105%, 110%, and 130%.

3. Comparisons of ISSR characteristics between the observations and various simulations

a. Relative humidity distributions with respect to temperature for clear-sky and in-cloud conditions

Comparisons of RHi distributions between the observations and simulations at various ranges of temperatures are used to investigate the overall occurrence of ISS in the simulations. The numbers of occurrences of RHi are shown for the 1-Hz observations and various simulations for in-cloud and clear-sky conditions (Figs. 3, 4). For the observations in both in-cloud and clear-sky conditions, only a few RHi occurrences are higher than the threshold of homogeneous nucleation based on Koop et al. (2000). This result is consistent with the findings of Cziczo et al. (2013), which showed that

TABLE 1. Characteristics of ISSRs for observations and various simulations.

Dataset	$\log_{10}(N_{\mathrm{ISSR}}) = a + b \times \log_{10}(L_{\mathrm{ISSR}})$ a and b values	$\log_{10}(N_{\mathrm{spacing}}) = a + b \times \log_{10}(L_{\mathrm{spacing}})$ a and b values	Percentage of ISS for in-cloud conditions	$\mathrm{RH}_{\max} = a + b \times \log_{10}(L_{\mathrm{ISSR}})$ a and b values	$\mathrm{RH}_{\mathrm{ave}} = a + b \times \log_{10}(L_{\mathrm{ISSR}})$ a and b values	$d\mathrm{RHi}_q$, $d\mathrm{RHi}_T$ contribution slope values	$d\mathrm{RHi}_q$, $d\mathrm{RHi}_T$ contribution ($d\mathrm{RH}_{\max} < 8\%$) slope values
Obs	0.77 ± 0.40	−0.004 ± 0.24	51.2	68.5 ± 2.6	89.7 ± 1.1	0.92 ± 0.006	0.88 ± 0.002
	−0.72 ± 0.10	−0.51 ± 0.05		12.9 ± 0.68	4.89 ± 0.29	0.071 ± 0.007	0.11 ± 0.002
250m-X	4.08 ± 0.41	4.50 ± 0.49	40.2	97.6 ± 1.7	99.5 ± 0.7	0.89 ± 0.001	0.79 ± 0.004
	−1.51 ± 0.10	−1.60 ± 0.12		2.25 ± 0.42	1.04 ± 0.18	0.087 ± 0.001	0.20 ± 0.004
250m-Dia	4.61 ± 0.49	3.14 ± 0.28	41.3	98.0 ± 1.4	99.7 ± 0.6	0.99 ± 0.002	0.78 ± 0.004
	−1.65 ± 0.12	−1.24 ± 0.06		2.15 ± 0.32	0.99 ± 0.14	0.052 ± 0.001	0.21 ± 0.004
250m-Y	4.20 ± 0.24	5.68 ± 0.48	50.6	118 ± 4	108 ± 2	1.51 ± 0.02	0.83 ± 0.006
	−1.56 ± 0.06	−1.95 ± 0.11		−1.80 ± 1.03	−0.45 ± 0.53	0.027 ± 0.001	0.16 ± 0.006
1km-X	4.78 ± 0.34	6.10 ± 0.49	42.8	97.5 ± 1.8	99.2 ± 0.8	1.17 ± 0.003	0.83 ± 0.006
	−1.54 ± 0.08	−1.85 ± 0.11		2.14 ± 0.40	1.05 ± 0.17	−0.067 ± 0.002	0.16 ± 0.006
4km-X	7.48 ± 0.9	5.77 ± 0.72	40.6	99.9 ± 3.6	95.5 ± 1.3	1.17 ± 0.007	0.74 ± 0.02
	−1.94 ± 0.19	−1.59 ± 0.15		1.50 ± 0.73	1.81 ± 0.27	−0.087 ± 0.007	0.25 ± 0.02
RH130–250m-X	3.58 ± 0.39	3.53 ± 0.31	45.5	72.5 ± 2.9	92.4 ± 1.2	0.81 ± 0.002	0.70 ± 0.003
	−1.35 ± 0.09	−1.34 ± 0.07		10.6 ± 0.7	3.74 ± 0.29	0.16 ± 0.002	0.29 ± 0.003
RH130–1km-X	4.48 ± 0.41	6.51 ± 0.67	50.2	69.1 ± 2.4	91.8 ± 1.3	0.90 ± 0.003	0.67 ± 0.005
	−1.44 ± 0.09	−1.95 ± 0.15		11.1 ± 0.5	3.86 ± 0.28	0.096 ± 0.002	0.32 ± 0.005
RH130–4km-X	4.94 ± 0.79	8.14 ± 1.3	50.2	60.6 ± 3.0	80.3 ± 1.6	1.08 ± 0.008	0.62 ± 0.022
	−1.36 ± 0.16	−2.11 ± 0.27		12.6 ± 0.6	6.40 ± 0.33	0.010 ± 0.007	0.36 ± 0.022
RH150–250m-X	2.89 ± 0.36	7.35 ± 0.31	49.2	62.2 ± 3.1	90.9 ± 1.6	0.81 ± 0.002	0.71 ± 0.003
	−1.16 ± 0.09	−1.36 ± 0.07		14.0 ± 0.7	4.51 ± 0.37	0.16 ± 0.001	0.28 ± 0.003
RHinf-250m-X	3.21 ± 0.44	3.55 ± 0.32	50.5	53.0 ± 3.1	90.8 ± 1.8	0.77 ± 0.001	0.70 ± 0.004
	−1.24 ± 0.10	−1.35 ± 0.08		17.3 ± 0.7	4.93 ± 0.43	0.17 ± 0.001	0.30 ± 0.004
EPSI0.1–250m-X	2.80 ± 0.40	2.97 ± 0.29	35.6	99.2 ± 1.8	98.5 ± 0.9	0.79 ± 0.002	0.82 ± 0.003
	−1.15 ± 0.10	−1.18 ± 0.07		1.98 ± 0.44	1.55 ± 0.23	0.16 ± 0.001	0.17 ± 0.003
IN0.5–250m-X	4.66 ± 0.71	4.25 ± 0.44	40.4	94.7 ± 1.6	97.5 ± 0.9	1.05 ± 0.002	0.75 ± 0.004
	−1.67 ± 0.18	−1.54 ± 0.11		3.00 ± 0.39	1.60 ± 0.23	0.026 ± 0.002	0.23 ± 0.004
RH130 + EPSI0.1 + IN0.5–250m-X	2.83 ± 0.50	3.01 ± 0.31	46.3	84.0 ± 2.3	99.8 ± 2.0	0.80 ± 0.002	0.73 ± 0.003
	−1.14 ± 0.12	−1.20 ± 0.07		8.45 ± 0.55	2.46 ± 0.46	0.16 ± 0.001	0.26 ± 0.003

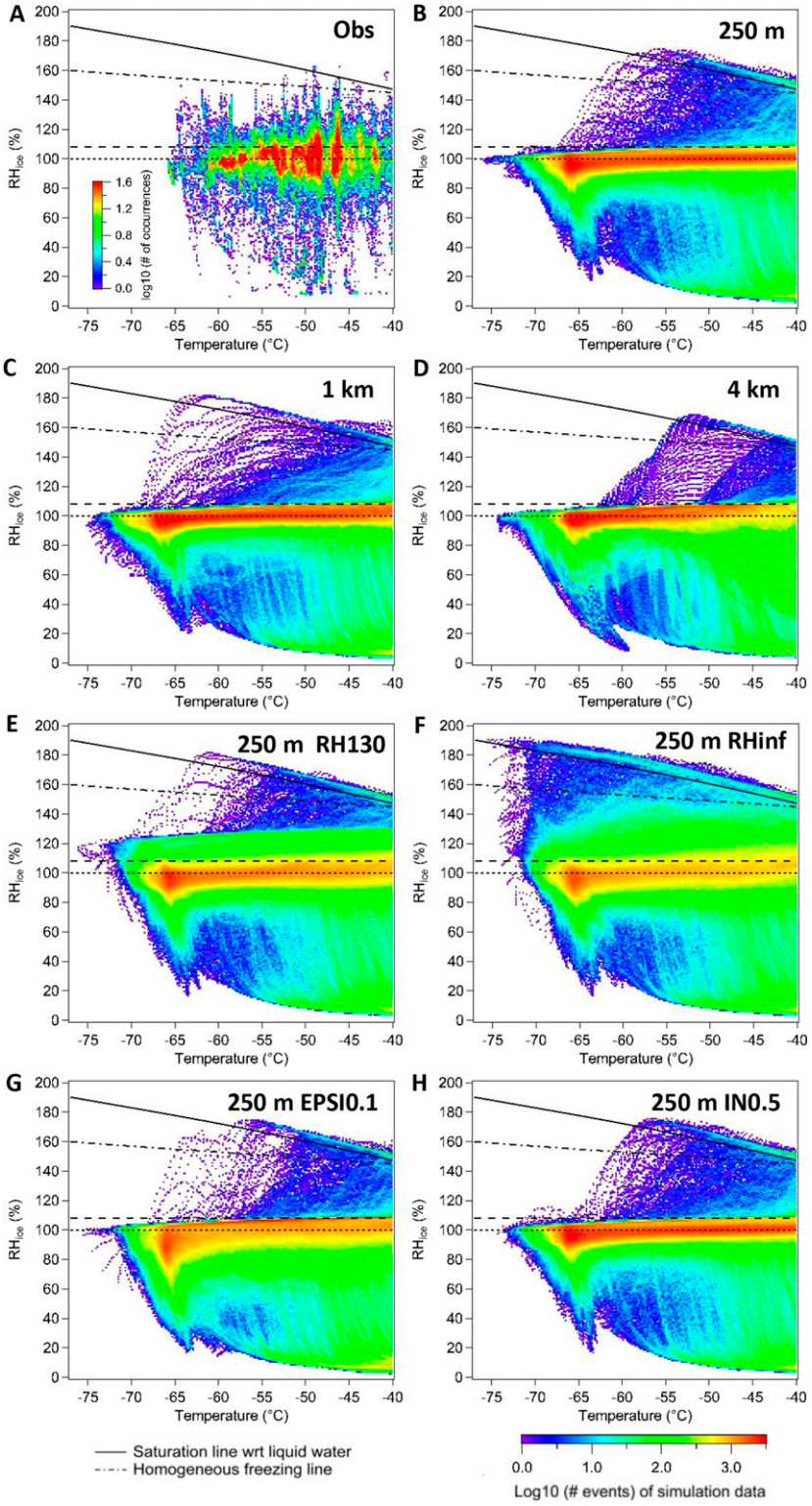

FIG. 3. RHi distributions for in-cloud conditions. (a) The 1-Hz observations from the DC3 campaign from −67° to −40°C; The control simulations at (b) 250-m, (c) 1-km, and (d) 4-km horizontal grid spacings. Simulations with modified microphysics at 250 m: (e) RH130, (f) RHinf, (g) EPSI0.1, and (h) IN0.5 runs. The black dotted and dashed lines denote RHi at 100% and 108%, respectively. The dotted–dashed line denotes the homogeneous nucleation line for aerosols at 0.5 μm (Koop et al. 2000), and the solid black line denotes liquid water saturation based on Murphy and Koop (2005). Color bars illustrate the log-scale number of 1-Hz observations and the log-scale number of mock aircraft samples in each RHi–T bin (i.e., 1% by 0.2°C).

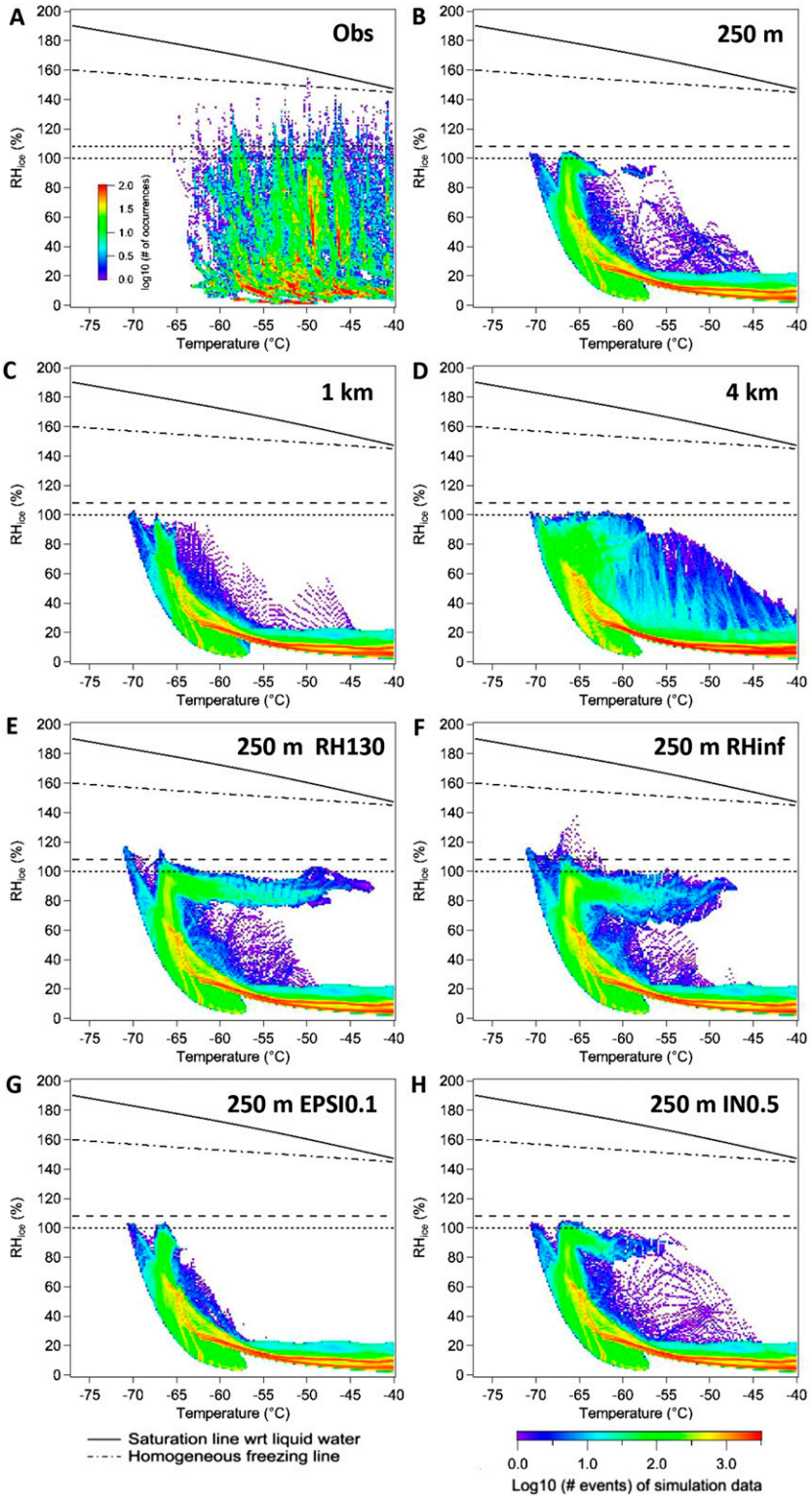

FIG. 4. As in Fig. 3, but showing RHi distributions for clear-sky conditions.

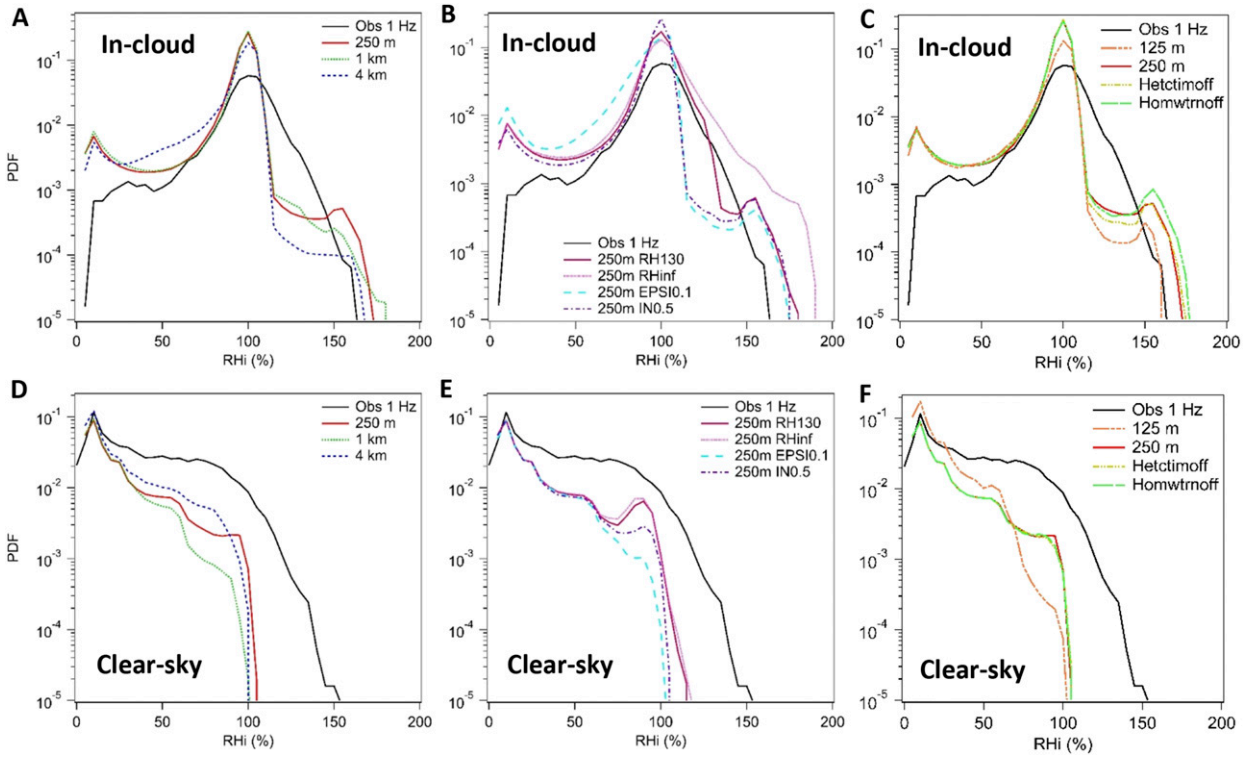

FIG. 5. Normalized frequency distributions of RHi for (a)–(c) in-cloud and (d)–(f) clear-sky conditions, binned by 5% of RHi.

most of the extratropical in situ observations of RHi are below the threshold of homogeneous nucleation from −40° to −70°C.

Results show that both the simulations and in situ observations have high occurrence frequencies of in-cloud RHi centered at 100% (Figs. 5a–c). This feature is consistent with the previous studies based on in situ and remote sensing observations (Diao et al. 2014a; Kahn et al. 2009; Ovarlez et al. 2002; Krämer et al. 2009). In addition, the peak of in-cloud RHi distribution centered at 100% is wider in the DC3 observations than those in the three ''control'' simulations (defined here as the simulations that use the unmodified microphysics scheme). The 4-km simulation shows more occurrences of in-cloud RHi around 25%–75% than the 0.25- and 1-km simulations, which is possibly attributable to weaker detrainment from convective cores at the coarser grid spacing (e.g., Bryan and Morrison 2012).

In contrast to the in-cloud conditions, the clear-sky RHi values in the three control simulations are almost exclusively below ice saturation, except for a few clear-sky ISS data in the 250-m control simulation (Fig. 4). The simulations generally have narrower peaks centered at 10% RHi distributions compared with the observations (Figs. 5d–f). Several factors may contribute to the narrower distribution range of RHi in the simulations. For example, the current CM1 simulations do not include radiative forcing or other synoptic-scale forcing (warm conveyer belts, anticyclones, jet streams, etc.), which have been previously reported to induce ISSR formation (Fusina and Spichtinger 2010; Diao et al. 2015; Spichtinger et al. 2005). Supporting this idea, real case simulations using the Weather Research and Forecasting (WRF) Model initialized with Global Forecast System (GFS) data show more occurrences of ISS for clear-sky conditions, and large sensitivities of ISS are seen in both clear-sky and in-cloud conditions when modifying the RHi threshold in the Cooper parameterization (D'Alessandro et al. 2017).

To examine the influences of the Cooper ice nucleation parameterization (Cooper 1986) on the simulated RHi distributions, we conducted a sensitivity test at 250-m horizontal grid spacing with a higher RHi threshold that increases the default RHi threshold from 108% to 130% (here named as RH130 run). By increasing the RHi threshold for initiating ice in the Cooper parameterization, one would expect to delay the initiation of new ice crystal formation and thereby increase the duration of time that ISS exists before it is depleted by water deposition on ice particles. Compared with the 250-m control simulation, the RH130 run allows

more in-cloud RHi between 108% and 130%, as well as slightly more clear-sky ISS. In another test completely inhibiting the Cooper parameterization from being activated (named the RHinf run), there are more occurrences of RHi above 130% in both in-cloud and clear-sky conditions. Other factors are examined by decreasing the water vapor deposition rate to one tenth of the default value (the EPSI0.1 run), and by decreasing the number of IN used in the Cooper parameterization to half of the default value (the IN0.5 run). However, neither of these two simulations increases the occurrence of higher ISS ($> 8\%$) as much as the RH130 and RHinf runs.

To further evaluate these conclusions, we also examined whether even smaller horizontal grid spacing or other modified ice microphysical processes would be able to increase the frequency of ISS above 8%. A $\Delta x =$ 125-m simulation with the default microphysics scheme and the mock aircraft speed of 125 m s^{-1} (here named the 125-m run) shows a similar PDF of RHi at temperature ≤ -40°C compared with the 250-m control simulation. No significant increase of the occurrence frequency of ISS $> 8\%$ at in-cloud and clear-sky conditions is seen (orange line in Figs. 5c,f). In addition, using $\Delta x = 250$ m, we conducted two more sensitivity tests to ice particle formation in the microphysics scheme, including 1) turning off the heterogeneous contact freezing and immersion freezing (named Hetctimoff) and 2) turning off the homogeneous freezing of cloud water and rain (named Homwtrnoff). These two simulations provide similar results to the 250-m control simulation and do not significantly increase the frequency distribution of ISS above 8% at in-cloud and clear-sky conditions. Slight increases are shown in the frequency of maximum ISS values near liquid saturation when the heterogeneous freezing or homogeneous freezing is turned off. This is likely because these freezing mechanisms only operate in conditions very close to liquid water saturation since cloud water only occurs in these conditions in the model and therefore would not have a direct impact on the distribution of RHi values below liquid saturation. In addition, several other factors may help to explain the small sensitivity of the occurrences of ISS $> 8\%$ to these two sensitivity tests, including the following: 1) the temperature restriction of our analysis to ≤ -40°C potentially limits the amount of liquid water surviving at this temperature range and 2) an upper limit (i.e., 300 L^{-1}) on total ice concentration in this microphysics scheme may restrain impacts from the heterogeneous and homogeneous freezing parameterization. Overall, these results reaffirm that the RHi threshold for initiating the Cooper parameterization has a major influence on allowing higher ISS in these simulations, while other ice microphysical processes play less important roles.

b. *Spatial scales of ice supersaturated regions*

We compare the one-dimensional horizontal extent of ISSRs sampled by the research aircraft with those sampled by the mock aircraft in the simulations. The distribution of the horizontal lengths of ISSRs has been previously reported to be represented by a power law, with more ISSRs occurring at smaller scales than at larger scales (Diao et al. 2014a; Gierens and Spichtinger 2000). The mean and median horizontal lengths of ISSRs are 3.1 and 0.7 km from the DC3 campaign, which are comparable to the previously reported values of 3.5 and 0.7 km, respectively, from the HIPPO campaign. The median length of ISSRs is also comparable to the median length of ~1 km for the horizontal scales of cirrus clouds sampled by research aircraft, calculated based on the cloud chord length distributions from Wood and Field (2011). Even though the smallest ISSR horizontal extent in the mock aircraft sampling of 0.25-, 1-, and 4-km simulations is 250 m (see section 2c), we calculate the mean and median horizontal lengths of the ISSRs equal or greater than 4 times the horizontal grid spacing ($4\Delta x$), which is the minimum horizontal scale resolved by the simulations (Bryan and Morrison 2012). The 250-m control simulation has mean and median ISSR horizontal lengths of 3.5 and 2.0 km, respectively, which are comparable to the observations.

Linear regressions are applied to ISSRs with horizontal extent $\geq 4\Delta x$ to further quantify the distributions of the ISSR horizontal lengths, where the slope value indicates the rate of decay for the ISSR occurrences as their horizontal extent increases (Fig. 6). Therefore, a larger absolute value of the slope indicates a relatively faster decay for the occurrences of larger ISSRs. Compared with the observations, all the simulations show faster decay for the occurrences of larger ISSRs, which means that simulations have relatively fewer occurrences of large ISSRs than the observations. In fact, the 0.25-, 1-, and 4-km control simulations with mock aircraft sampling in the cross-line direction (run-X in Table 1) show slopes of ~−1.51, −1.54, and −1.94, respectively, which are at least twice that from the observations (~−0.72). Sensitivity tests on the mock aircraft sampling directions show that the 250-m control simulation sampled in diagonal- or along-line directions have slopes of −1.65 and −1.56, respectively, which are both comparable to the slope of −1.51 in the 250 m-X run.

The patchiness of the spatial distributions of ISSRs is not only represented by their horizontal scales but also their spacings (i.e., the horizontal distance between individual ISSRs) (Fig. 7). The 0.25-, 1-, and 4-km control

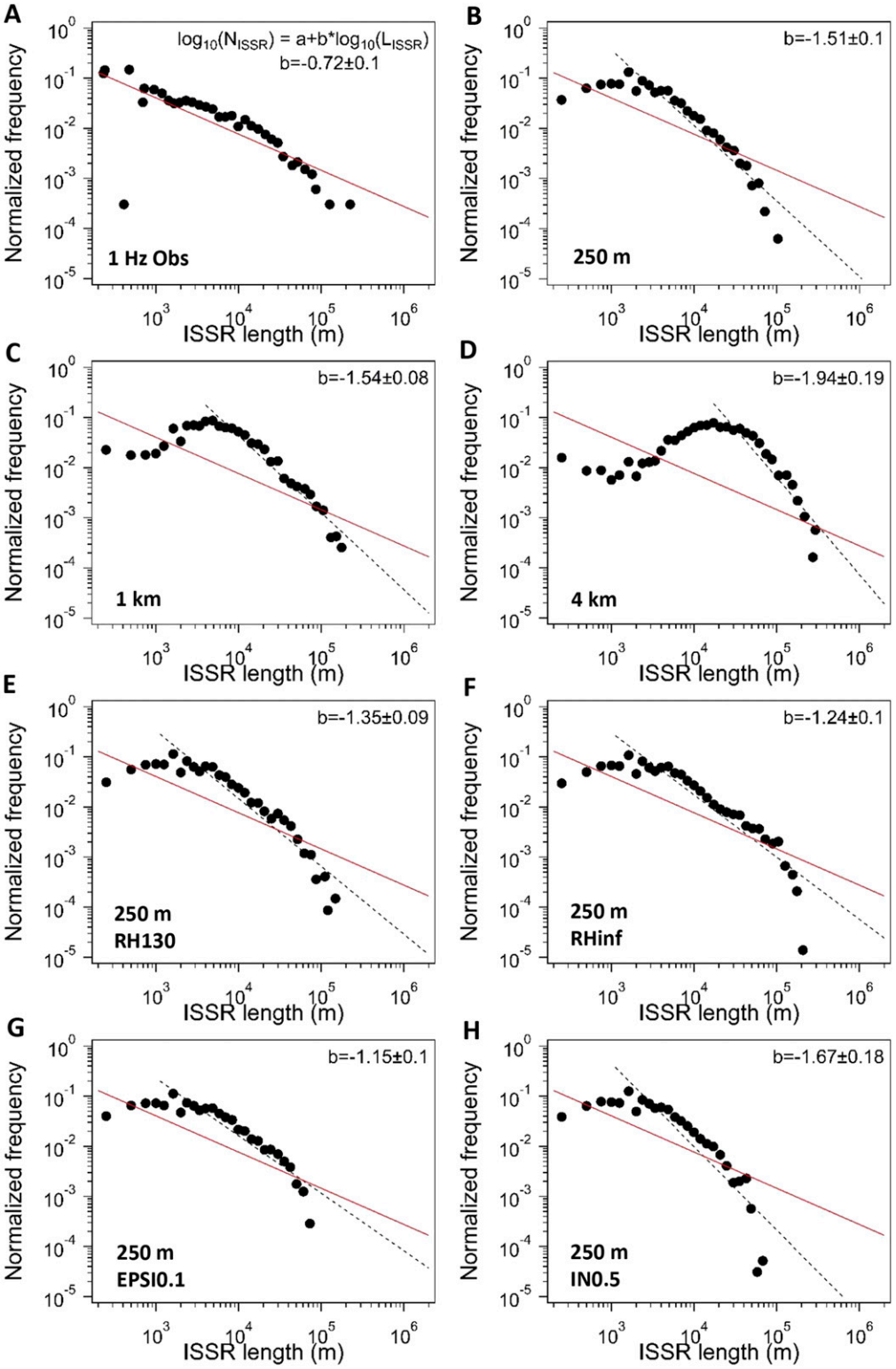

FIG. 6. Normalized frequency distributions of the ISSR horizontal extent. The lengths of ISSRs are binned on the log scale by $2^i, 2^{i+1}, 2^{i+2}, \ldots$, and the black dots represent the average ISSR lengths in each bin. Linear fits for the relationship between the ISSR horizontal lengths L_{ISSR} and their normalized frequencies N_{ISSR} are applied: $\log_{10}(\mathrm{N_{ISSR}}) = a + b \times \log_{10}(L_{\mathrm{ISSR}})$. The slopes are shown in the figure legend with ± 1 standard deviation. Red solid and black dashed lines denote the linear fits for the observations and simulations, respectively. Only horizontal extent of ISSRs or their spacings $\geq 4\Delta x$ are used for linear fits in Figs. 6–9.

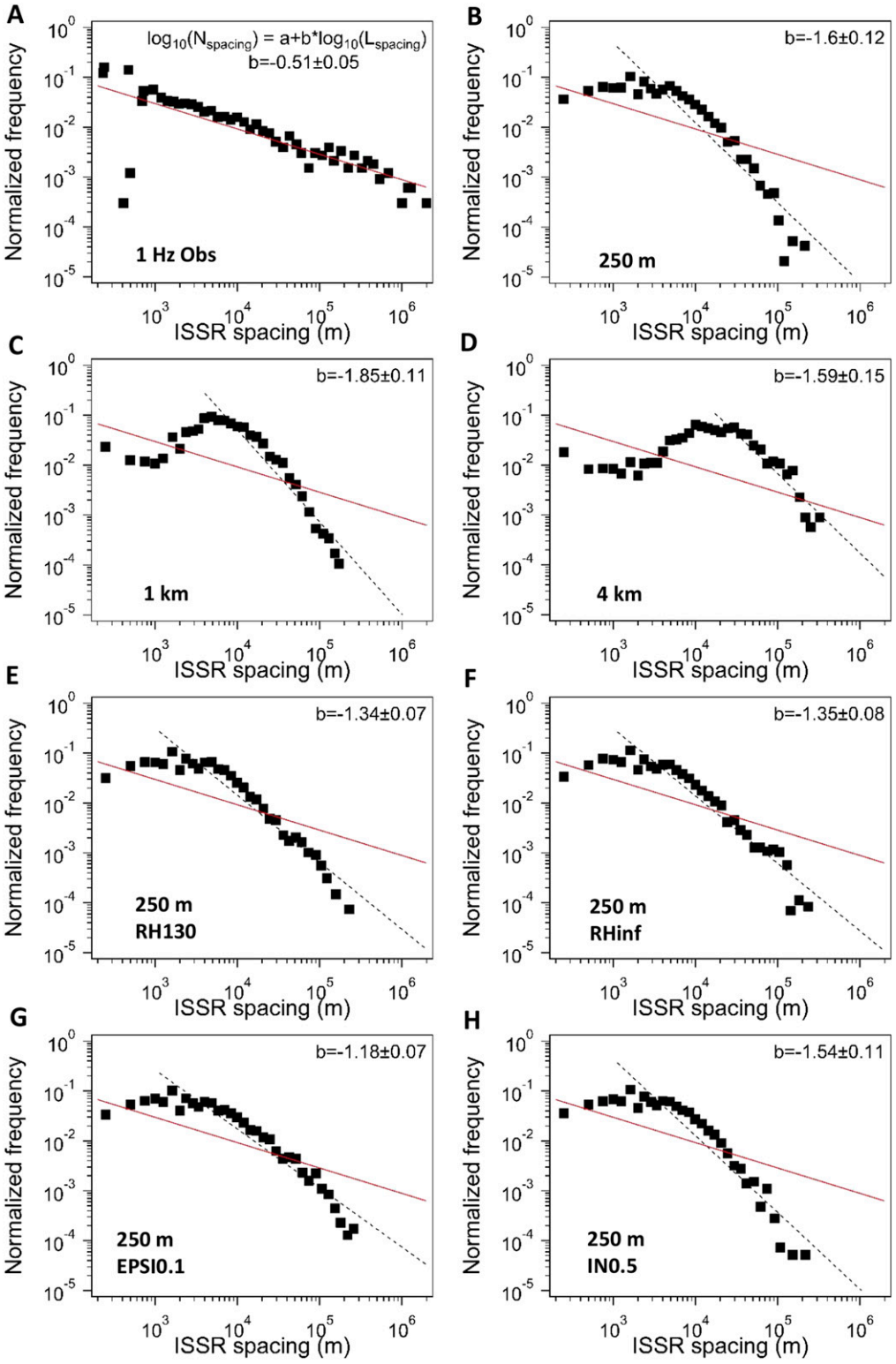

FIG. 7. As in 6, but for the normalized frequency distributions of the horizontal spacings between individual ISSRs. Linear fits are calculated for the relationship between the lengths of spacings between ISSRs (L_{spacing}) and their normalized frequencies (N_{spacing}): $\log_{10}(N_{\text{spacing}}) = a + b \times \log_{10}(L_{\text{spacing}})$.

simulations all show much faster decay in the distributions of ISSR spacings with slope values (i.e., −1.60, −1.85, and −1.59, respectively), at least triple that from the observations (slope = −0.51).

For both the distributions of ISSR horizontal extent and spacings, only minor improvements are shown by increasing the RHi threshold to 130% and 150% or by completely inhibiting the initiation of the Cooper parameterization (RH130, RH150, and RHinf runs, respectively) (Table 1). Similarly, only minor improvements in the linear fits are shown by the EPSI0.1 run or by combining three modifications (the RH130 + EPSI0.1 + IN0.5 run), while no significant changes are shown in the IN0.5 run. The lack of large-scale forcing (e.g., mesoscale uplifting and radiative cooling) may decrease the occurrences of larger ISSRs, in addition to the size limit of the simulation domain. On the other hand, improvements are shown by the RH130, RH150, and RHinf runs when analyzing the horizontal spatial fractions of in-cloud ISS with respect to the total in-cloud conditions (Table 1). These three runs show ISS fractions of 46%, 49%, and 51%, respectively, which are more comparable to the observations (51%) than the 250-m control simulation (40%). We note that these results only apply for the horizontal characteristics of ISSRs as a result of the aircraft's horizontal components' true airspeed being much greater in magnitude than that of the vertical components; therefore, evaluating the 3D structure of ISSRs would require additional observational datasets with alternative sampling techniques.

c. *The maximum and average RHi values for individual ISSRs*

The RHi in ISSRs plays a major role in determining the formation and growth of ice crystals. The relationships between the maximum and average RHi values (here named as RH_{max} and RH_{ave}, respectively) inside each ISSR and the log-scale horizontal length of that ISSR are quantified by linear regressions (Figs. 8, 9). Consistent with the previous analyses on the HIPPO dataset (Diao et al. 2014a), both the DC3 observations and the simulations show increases in RH_{max} (or RH_{ave}) with increasing ISSR horizontal lengths. These positive relationships are likely a result of adiabatic uplifting and/or radiative cooling of air parcels, since the cooling effects can lead to both the increase in RHi magnitudes and the expansion of ISSRs. However, compared with the observations, the 0.25-, 1-, and 4-km control simulations all show a weaker relationship between RH_{max} and the log-scale ISSR lengths, represented by much smaller slope values for the linear fit in Table 1 (i.e., 2.25, 2.14, and 1.50, respectively) than the observed one (12.9). Thus, as the ISSR horizontal lengths increase from 1 to 100 km, the RH_{max} on average increases from ~105% to 130% in the observations, while the RH_{max} in the control simulations only increases from ~103% to 108%.

To examine whether the simulated RH_{max} is dependent on the RHi threshold used for the Cooper parameterization, we apply linear regressions to the RH130 runs (Fig. 8e). The RH130–250m-X run shows a relationship between RH_{max} and ISSR horizontal lengths (slope = 10.6) much more similar to the observations. Such improvement in the simulated relationship between RH_{max} and ISSR horizontal lengths cannot be reproduced by modifying other factors, including changing the sampling directions, decreasing the water vapor deposition rate, or decreasing the IN number concentration from the Cooper parameterization (Table 1). In addition, the RH150 and RHinf runs show continuous increases in the slope values to 14.0 and 17.3, respectively, which further confirms the impacts of revising the RHi threshold for initiating the Cooper parameterization on these relationships.

Similarly, the control simulations at all three horizontal grid spacings show weaker relationships between RH_{ave} and ISSR horizontal lengths (slopes ranging from 1.04 to 1.81) than the observations (slope = 4.89). Consistent with the analyses of RH_{max}, the RH130, RH150, and RHinf runs at 250 m are the only ones that give improved relationships between RH_{ave} and the log-scale ISSR lengths with slope values of 3.74, 4.51, and 4.93 in Table 1, respectively.

d. *ISSR formation condition: Contributions from water vapor and temperature spatial heterogeneities*

The locations of ISSR formation are predominantly affected by spatial heterogeneities in the RHi field, which are fundamentally determined by the spatial distributions of water vapor and temperature. We examine whether there is a scale dependence for the formation mechanism of ISSRs, based on the contributions of water vapor and temperature spatial heterogeneities represented in the simulations at various horizontal grid spacings. Eulerian-view samples of ISSRs are analyzed for both observations and simulations, with all the observed ISSR samples restricted to near-isobaric levels (ΔPressure < 1 hPa) in order to be comparable to the isobaric mock aircraft sampling in the simulations.

The contributions of water vapor and temperature spatial heterogeneities (named $d\mathrm{RH}_q$ and $d\mathrm{RH}_T$) are quantified in terms of their contributions to the magnitudes of higher RH_{max} values ($d\mathrm{RH}_{max}$) inside individual ISSRs based on the calculations in Diao et al. (2014a). Here $d\mathrm{RH}_{max}$ is calculated by comparing the

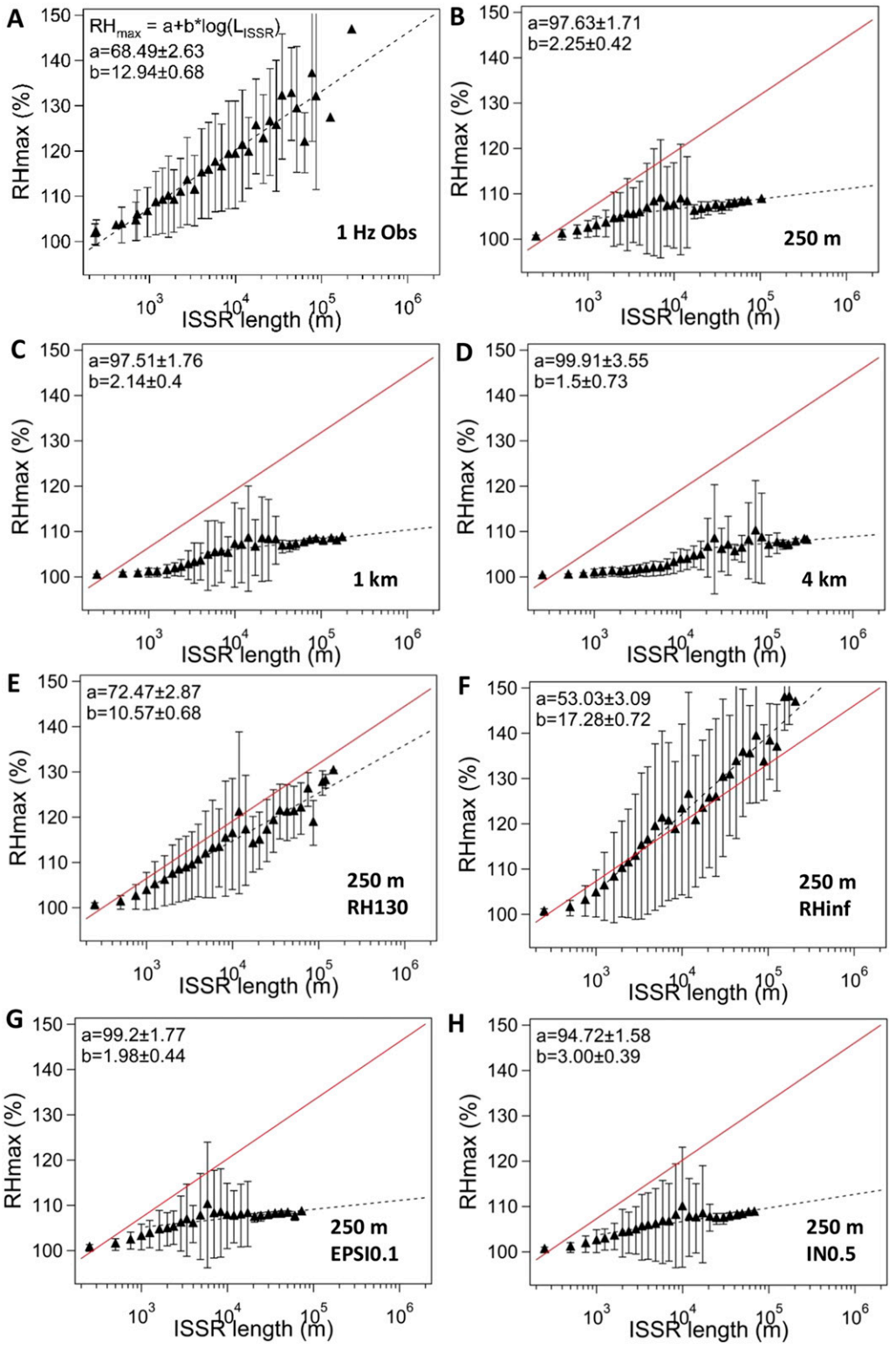

FIG. 8. Distributions of the RH_{max} inside the ISSRs in relation to the lengths of ISSRs. The bin sizes of L_{ISSR} follow those in Fig. 6. Linear fits are calculated for: $RH_{max} = a + b \times \log_{10}(L_{ISSR})$. (b)–(h) Red solid and black dashed lines denote the linear fits for observations and simulations, respectively.

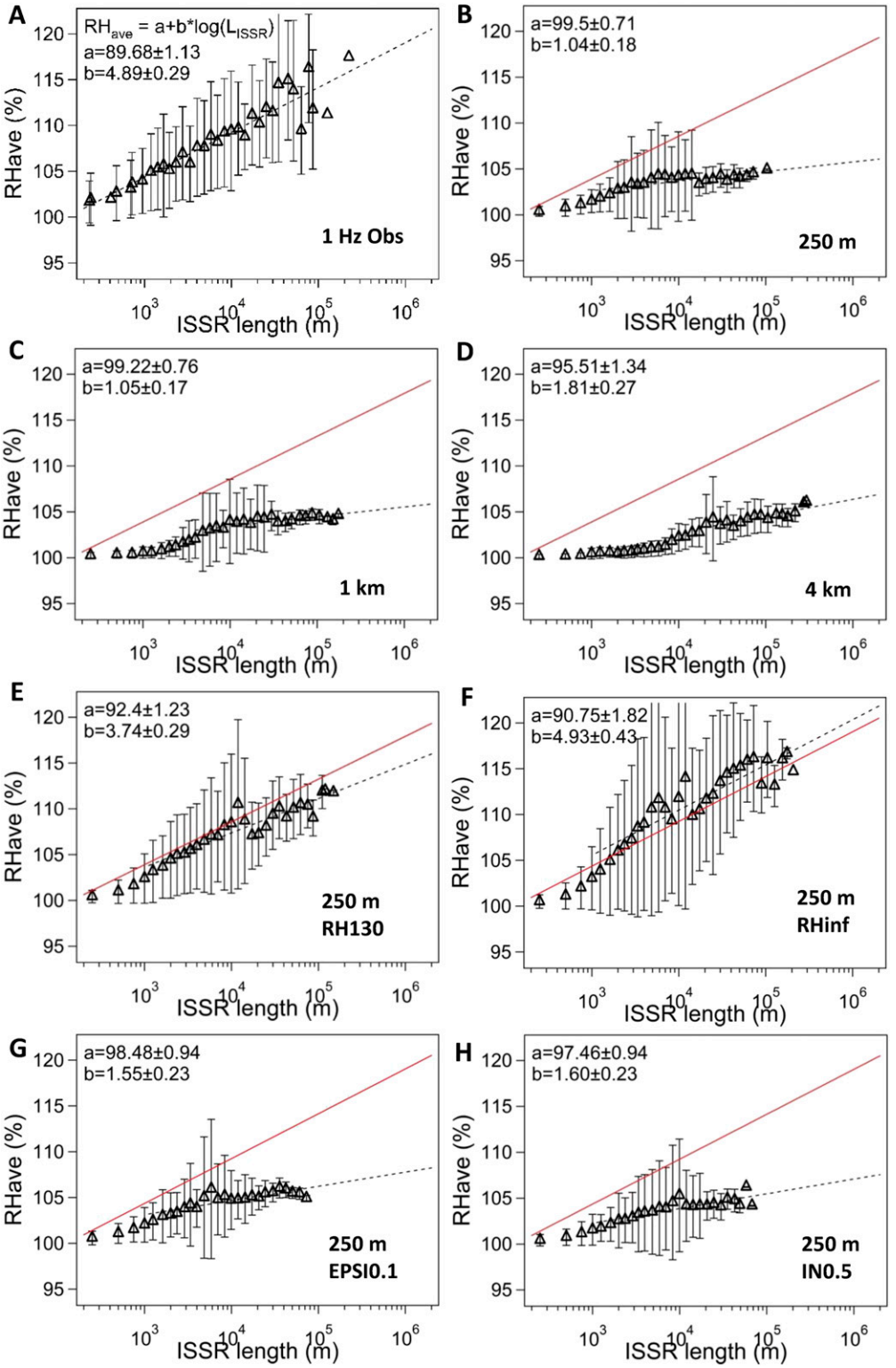

FIG. 9. As in Fig. 8, but for distributions of RH_{ave} inside the ISSRs. Linear fits are calculated for $RH_{ave} = a + b \times \log_{10}(L_{ISSR})$.

RH_{max} in ISSRs with their adjacent, subsaturated surroundings, following the definition in Diao et al. (2014a). Linear fitting is applied to dRH_q and dRH_T for all ISSR samples (Fig. 10). The slopes of linear fits for dRH_q and dRH_T in the 250-m control simulation represent that the average fractions of dRH_{max} in ISSRs contributed by water vapor and temperature spatial heterogeneities are 0.89 and 0.087, respectively. These contributions are consistent with the slope values of 0.92 and 0.071 in the DC3 dataset (Table 1). The dRH_q and dRH_T contributions do not exactly sum up to unity because of the total derivative approximation used in the calculations, as explained in Diao et al. (2014a). These results are also consistent with the dominant contribution from water vapor spatial heterogeneities based on the HIPPO data at various latitudes, longitudes, and altitudes (Diao et al. 2014a).

The main difference between the observations and simulations is the large variabilities in the dRH_q and dRH_T, as shown in the simulations. The 1- and 4-km control simulations show even higher water vapor contributions greater than one (slopes of 1.17 and 1.17), with negative temperature contributions of −0.07 and −0.09, respectively. These larger variabilities in the simulations are likely as a result of the larger fluctuations in vertical velocity (discussed in section 4c), while aircraft generally avoid sampling the convective core regions. When restricting the linear fit to below the RHi threshold of the Cooper parameterization (i.e., $dRH_{max} \leq 8\%$), the 4-km simulation shows about a 15% smaller contribution from dRH_q (slope = 0.74) than the observations (slope = 0.88) (Table 1). Such scale dependence for the average contributions from water vapor and temperature spatial heterogeneities is not seen in the observations, when the observation dataset is averaged from 250 m to up to 100-km horizontal scales (Diao et al. 2014a). Thus, even though the dominant contributions from water vapor spatial heterogeneities are represented in all of the simulations, further investigation is needed to examine the causes behind such scale dependence in the formation mechanisms of ISSRs.

4. Comparisons on ISSRs and ice microphysical properties in an evolutionary view

a. *Occurrences of five cirrus evolution phases*

Comparing the evolution of ice clouds between observations and model simulations requires one to extract information from the Eulerian view-based observations to derive an evolutionary view of the clouds. We use the five evolution phases of ISSRs and ICRs as defined in Section 2, based on the previous method of Diao et al. (2013b). This method mainly provides a statistical comparison between simulations and observations by representing the spatial relationship between ISSRs and ICRs, while we note that the ISSRs and ICRs in MCSs do not necessarily follow the exact evolution trend from phases 1 to 5.

The occurrence frequencies of the five evolutionary phases are quantified for both the observations and simulations (Figs. 11a,b). The 250-m control simulation captures a few clear-sky ISSRs (phase 1), while the 1- and 4-km control simulations show near-zero occurrences of phases 1 and 2. For simulations with the modified microphysics schemes, the 250-m RH130 run shows a higher probability of clear-sky ISSRs at 0.096 than the control simulation (0.051), which is also closer to the observed value of 0.12. All of the simulations capture the latter phases (phases 3, 4, and 5), with higher probability of the later growth phase, and lower probability of the sedimentation phase, compared with the observations. These differences could be because the RHi and ice crystal distributions in the observations are more inhomogeneous than the simulations. It is also possible that the simulations have not been integrated long enough.

In addition, the spatial ratio of ICR/ISSR is examined as an indicator of the expansion of ICRs relative to ISSRs. Initially, the ICR/ISSR spatial ratio is smaller than 1, since ICRs are smaller than ISSRs in the earlier phases. Eventually the ratio becomes larger than 1 as ICRs expand in space (Figs. 11c,d). The observations show that the distribution of the ICR/ISSR spatial ratio peaks at one, indicating that, when ICRs and ISSRs coexist, the majority of them have similar spatial scales. For all of the simulations, the peak positions of the ICR/ISSR spatial ratios are greater than 1, and the 4-km simulation deviates the most from the observations, indicating that the simulations have relatively larger ICRs and relatively smaller ISSRs when they coexist. Even though the RH130 run allows for higher probabilities of the earlier phases, it does not improve the spatial ratio of ICR/ISSR, as it still overestimates the horizontal extent of ICRs with respect to ISSRs.

b. *Comparisons on the evolution of RHi, Nc, and IWC for the five cirrus evolution phases*

After separating the five evolution phases, the analyses of RHi, Nc, and IWC for the individual phases are shown in Figs. 12, 13, and 14, respectively. The evolution trend of these ice microphysical properties is analyzed with respect to the horizontal extent of the ISSR + ICR samples (defined as spatially continuous regions that are either ice supersaturated or with ice crystals). The horizontal extent of ISSR + ICR generally increases during

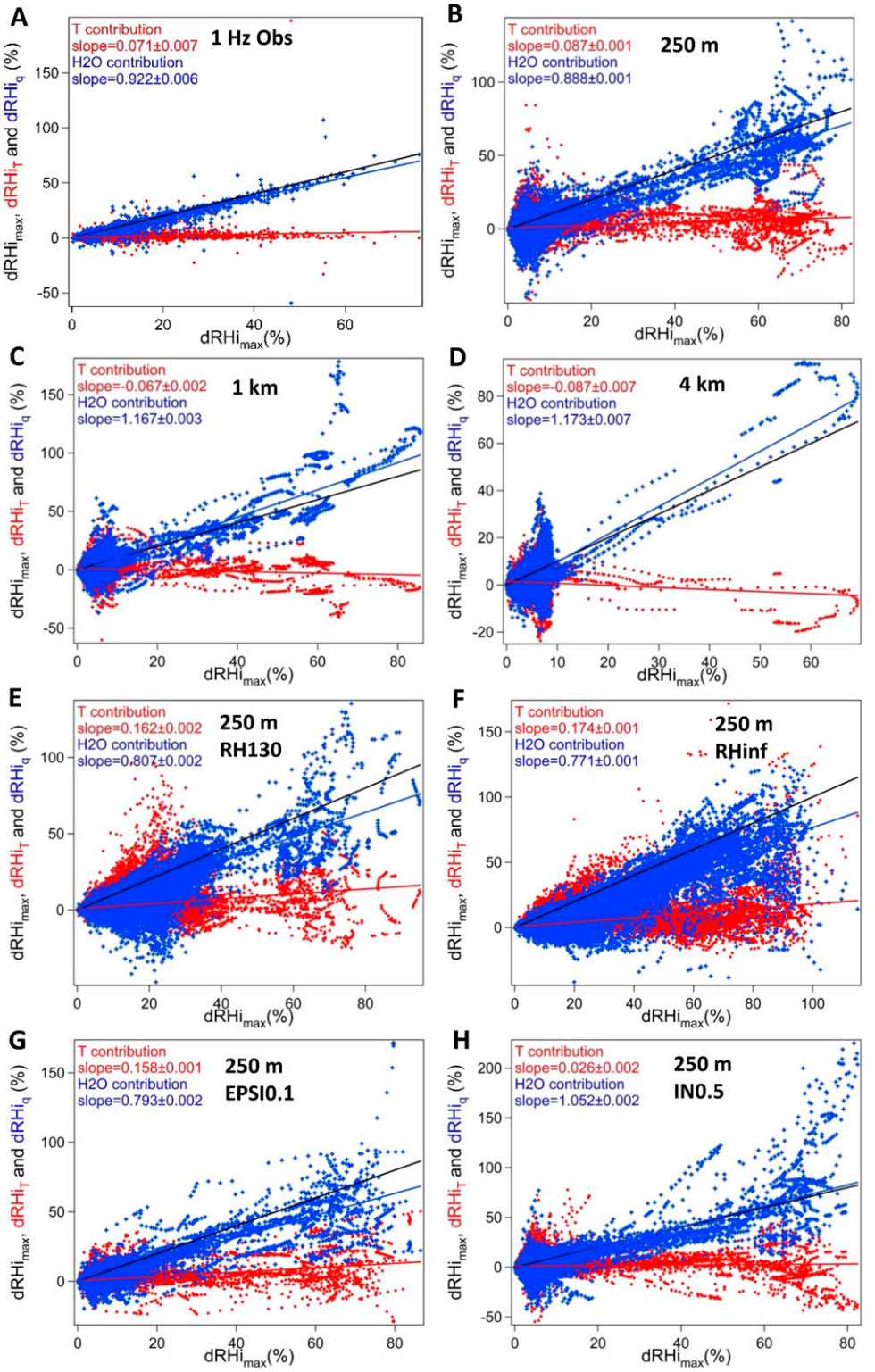

FIG. 10. Contributions of water vapor and temperature spatial heterogeneities to the magnitude of the maximum RHi difference ($d\mathrm{RHi}_{\max}$) between ISSRs and the adjacent subsaturated conditions. Contributions from the water vapor spatial heterogeneities ($d\mathrm{RHi}_q$) and temperature spatial heterogeneities ($d\mathrm{RHi}_T$) are denoted in blue and red dots for individual ISSRs with linear fits in blue and red lines, respectively. The black line denotes the 1:1 line.

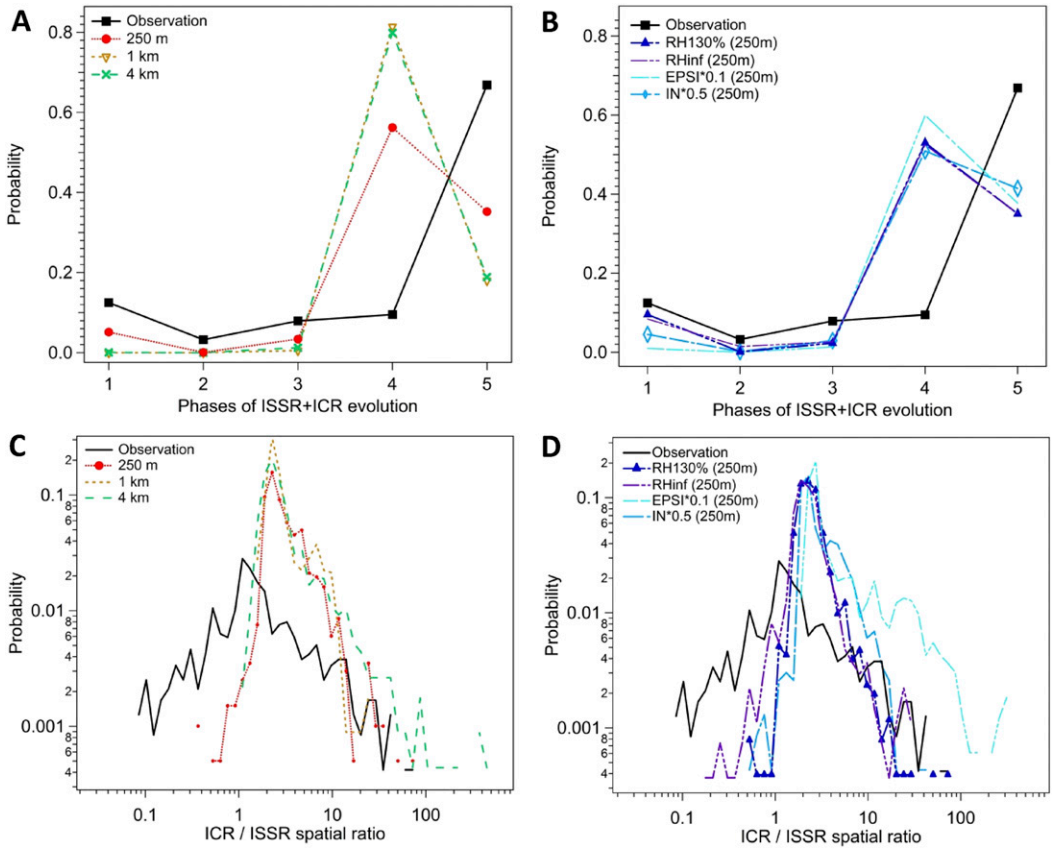

FIG. 11. Probabilities of (a),(b) the five evolution phases for ISSRs and ICRs and (c),(d) the spatial ratios for ICR/ISSR for phases 2–4.

the earlier phases; then, when all the ISS is depleted, the ICRs dissipate, and therefore their sizes decrease.

The evolution of the average RHi in each ISSR + ICR sample is shown in Fig. 12. The simulations can capture the general evolution trend of RHi distributions in the observations; that is, the average RHi increases with the increasing extent of clear-sky ISSRs, which is consistent with the formation of ISSRs during adiabatic or diabatic cooling. Once ice crystals form, the average RHi decreases because of the depletion of water vapor by ice crystal formation and growth in phases 2–4. Last, in the sedimentation phase, as ice crystals sediment into drier conditions, both the spatial extent of ICRs and the average RHi decrease. The simulations are also able to capture the wide range of RHi distributions in the sedimentation phase extending from slightly below saturation to drier conditions, because of the sedimentation of ice crystals at various sizes into different levels. Different from the observations, the 250-m control simulation shows that the average RHi is confined to below 105% for phases 1–4, compared with the RHi values up to 130% in the observations.

We further compare the evolution of the average Nc and IWC for the in-cloud segments in Figs. 13 and 14. The observations show that both Nc and IWC increase with increasing extent of ISSR + ICR samples for phases 2–4, and then both decrease in the sedimentation/sublimation phase. Similar relationships between Nc (or IWC) and the lengths of ISSR + ICR are also evident from the simulations, but with relatively narrower distribution ranges of the average Nc and IWC. When ICRs coexist with ISSRs, the observations and the 250-m simulation show the average Nc around 0.03–200 and 20–300 L^{-1}, respectively. Similarly, for the sedimentation phase, the observations and 250-m control simulation show Nc around 0.03–100 and 1–100 L^{-1}, respectively. In addition, compared with the observations, the 250-m control simulation shows fewer samples of average IWC from around 3×10^{-4} to 0.005 g m^{-3}. These results indicate a lack of variabilities for the average Nc and IWC inside in-cloud segments during the evolution of ISSRs and ICRs in the 250-m control simulation. The 250 m RH130 run improves the evolution of Nc by providing more occurrences in that

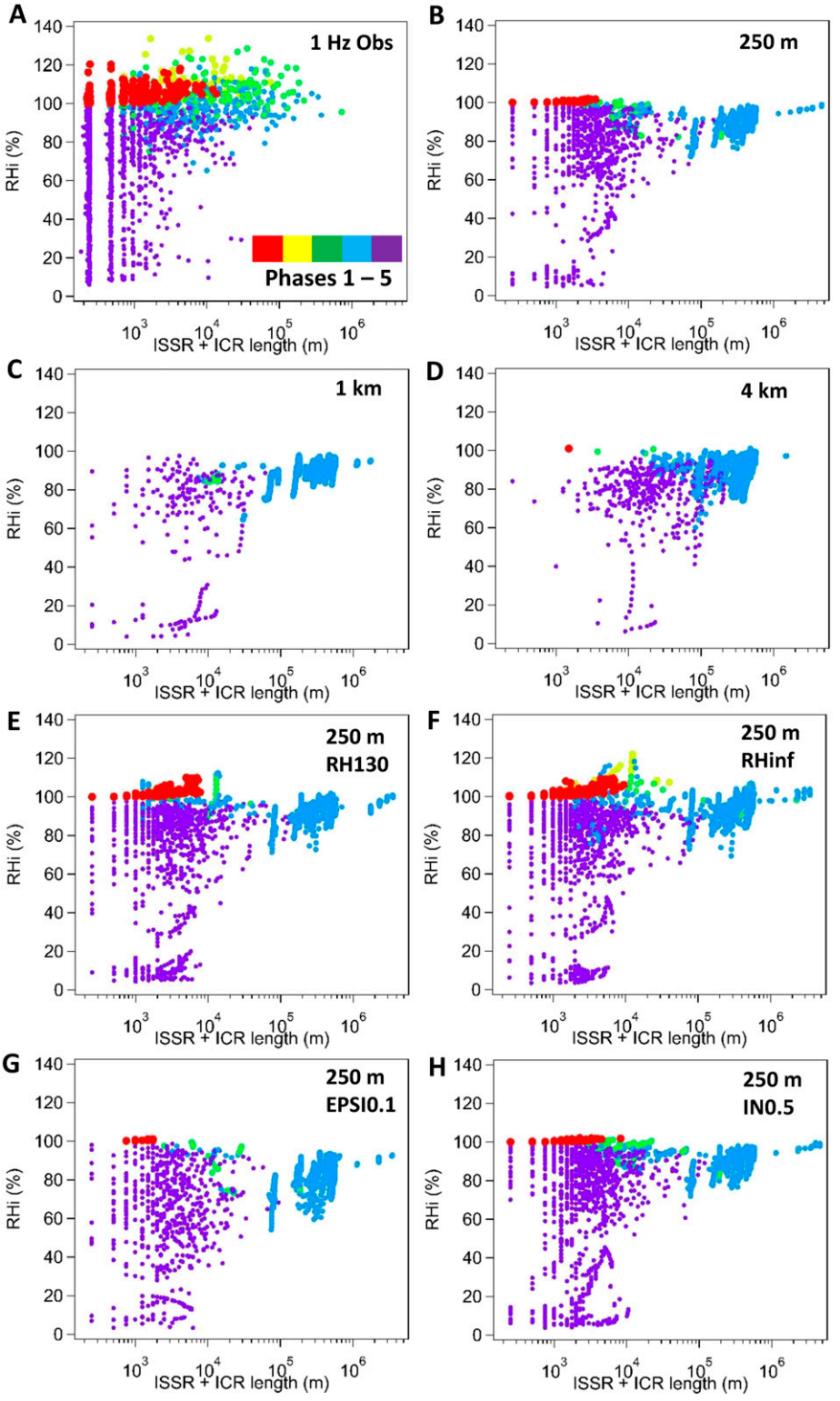

FIG. 12. The evolution trend of the average RHi values inside ISSR + ICR samples during the five evolution phases.

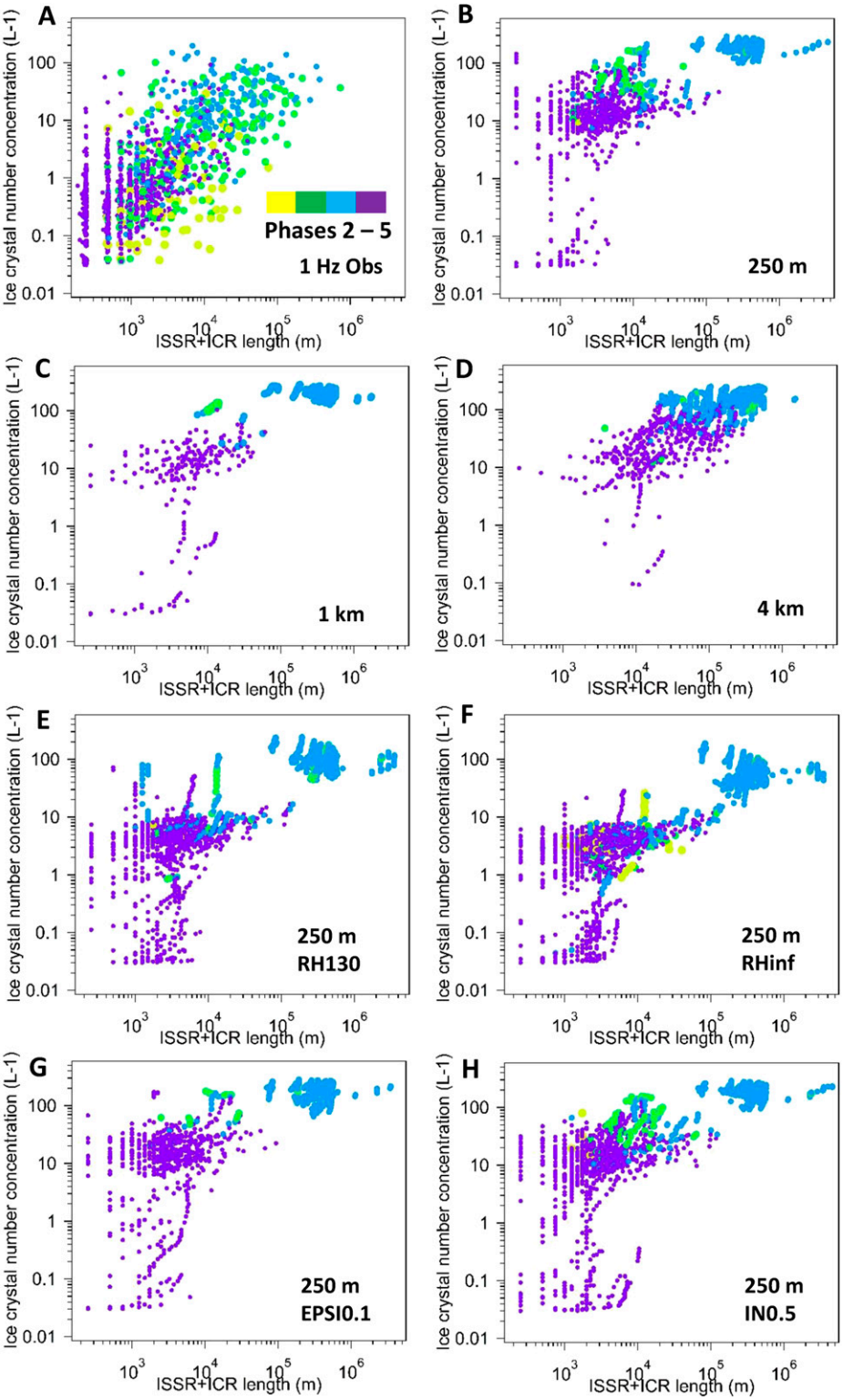

FIG. 13. The evolution trend of the average Nc values inside in-cloud segments during phases 2–5.

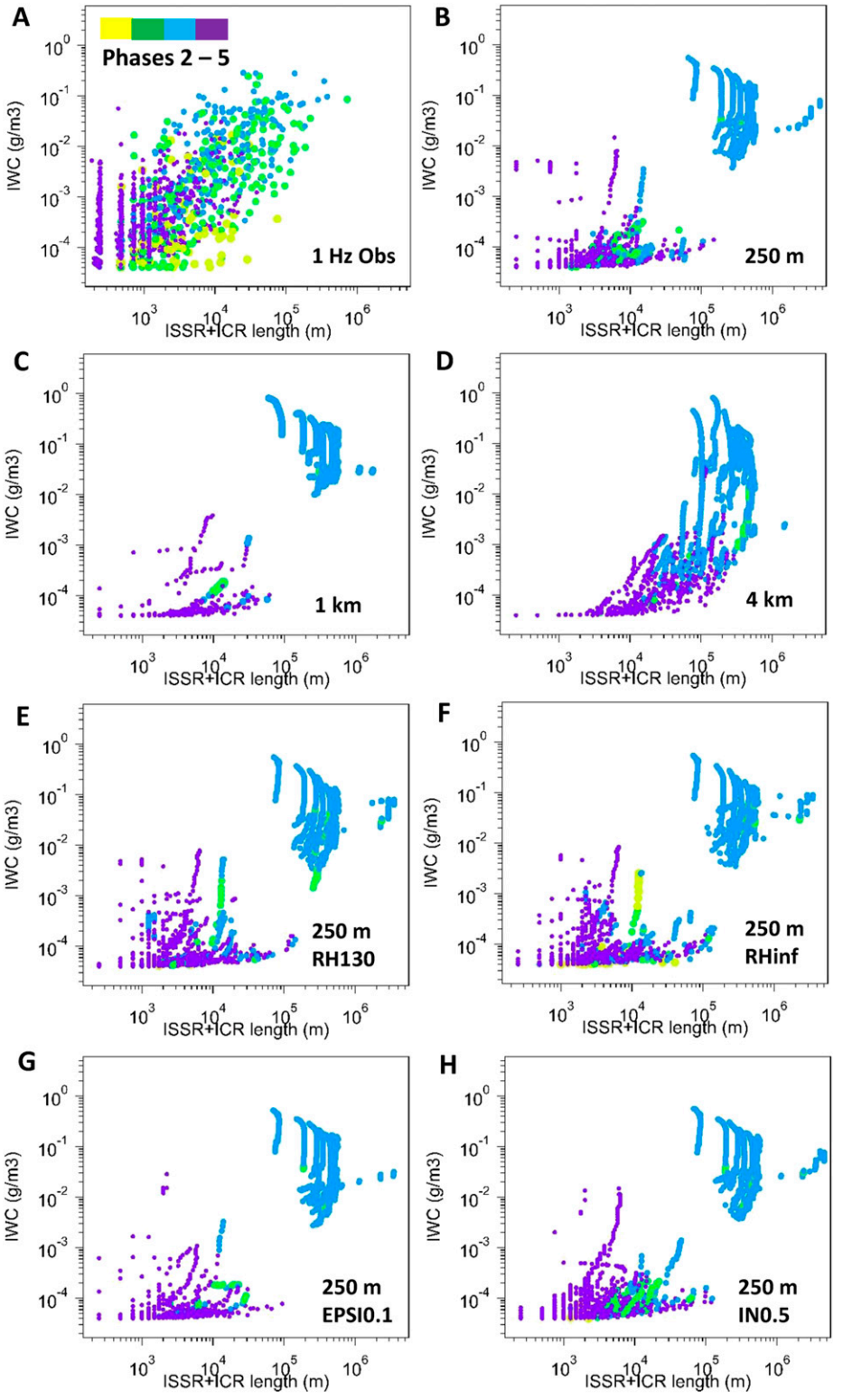

FIG. 14. As in Fig. 13, but for the evolution trend of the average IWC values.

range (0.1–10 L^{-1}), yet it does not improve the evolution of IWC significantly. When completely turning off the Cooper parameterization, the magnitude of average Nc for the early growth phase is significantly reduced (Fig. 13f). Note that the simulated Nc and IWC represent a wider size range of ice hydrometeors (i.e., cloud ice, snow, and graupel) compared with the Fast-2DC measurements (67.5–1600 μm), suggesting that simulations may have further underestimated the variabilities of Nc and IWC when considering ice particles smaller or larger than the measurement range. In addition, the GV aircraft avoided sampling the convective core region and therefore may underestimate the maximum Nc and IWC, but this cannot explain the lack of variability in these values in the simulations. The reason for the wider Nc and IWC ranges in the observations than the simulations is likely due to the heterogeneous distributions of ice crystals in the observations that are not captured by the simulations, leading to spatial heterogeneities in the fall speeds of ice crystals and their sublimation rates in the observations. We speculate that the lack of heterogeneity in the model is possibly because of the lack of heterogeneity in the IN concentration for a given temperature based on the Cooper parameterization, while the exact cause(s) requires further investigation.

c. *Impacts on dynamical conditions by modifying the Cooper parameterization*

To examine the impacts of modifying the Cooper parameterization on the dynamical conditions of the MCS, the distributions of vertical velocity are shown for the five evolution phases as well as for ISS and non-ISS conditions (Fig. 15). All the simulations show similar normalized frequency distributions of vertical velocity compared with the observations, except for very few occurrences of phases 1 and 2 in the 1- and 4-km control simulations. We note that the temperature distributions in the observations mostly occur from around −40° to −60°C, while the simulation outputs mostly range from −60° to −70°C, but this cannot explain the fewer occurrences of phases 1 and 2 in the simulations since the occurrence frequency of ISS does not vary significantly with temperature based on the DC3 data. The average vertical velocity $\overline{w}$ is examined in relation to Nc and IWC, and it is almost always higher in the ISS than the non-ISS conditions. The absolute $\overline{w}$ increases with the increasing Nc and IWC and shows much higher updrafts and downdrafts in the simulations than the observations, likely because of the aircraft sampling avoiding convective core regions. Thus, we further compare all the simulations with respect to the 250-m control simulation for large Nc and IWC. The 1- and 4-km simulations show smaller absolute $\overline{w}$ for large Nc and IWC compared with the 250-m control simulation. The RH130 run shows similar range of $\overline{w}$, with slightly larger $\overline{w}$ (up to 7 m s^{-1}) compared with the 250-m control simulation (up to 5 m s^{-1}) for the ISS with large Nc. However, the RH150 run shows much higher $\overline{w}$ (up to 35 m s^{-1}) than the 250-m control simulation (up to 9 m s^{-1}) for ISS with large IWC, indicating that large IWC in the RH150 run is sometimes associated with high updraft speeds, potentially because of the allowance of too many high RHi values.

5. Discussion

The comparisons between idealized simulations and in situ observations in this study are focused on general statistical distributions of RHi and ice microphysical properties, which have been consistently seen in various field campaigns, including the DC3 dataset in this work and two other campaigns in Diao et al. (2013b) and Diao et al. (2014a). Thus, it is not the intention of this study to simulate the exact same dynamical conditions as observed in individual research flights, but rather to provide a statistically robust comparison by using composite datasets of in situ observations and simulations.

Simulations with $\Delta x = 250$ m are mainly examined in this study, comparable to the horizontal resolution of 1-Hz in situ observations onboard the NSF GV aircraft in the DC3 campaign. Among the three horizontal grid spacings used in the model, the 1-km simulation shows similar results to the 250-m simulation for representing the ISSR characteristics, including the distributions of ISSR horizontal extent, the relationships of RH_{max} and RH_{ave} with ISSR lengths, and the ISSR formation contributed by water vapor and temperature spatial heterogeneities. Bryan et al. (2003) showed that 1-km grid spacing is not yet sufficient to represent the inertial subrange of turbulence, and thus sub-1-km simulations may be needed. Bryan et al. (2003) mentioned that certain properties of the simulated squall line (e.g., the squall line structure and mass transport) are qualitatively similar for simulations at various horizontal grid spacings, while other factors (e.g., the intensity and rate of precipitation) are found to be more sensitive to the horizontal grid spacings. To determine whether the 250-m grid spacing is sufficient enough to provide a convergence for the statistical distributions of ISSR characteristics requires future analyses at even smaller horizontal grid spacings (e.g., ~100 and sub-100 m). The smallest horizontal grid spacing used in this work is 125 m, which shows no significant increase of the occurrence frequency for ISS > 8% compared with 0.25-, 1-, and 4-km simulations. Thus, we speculate that

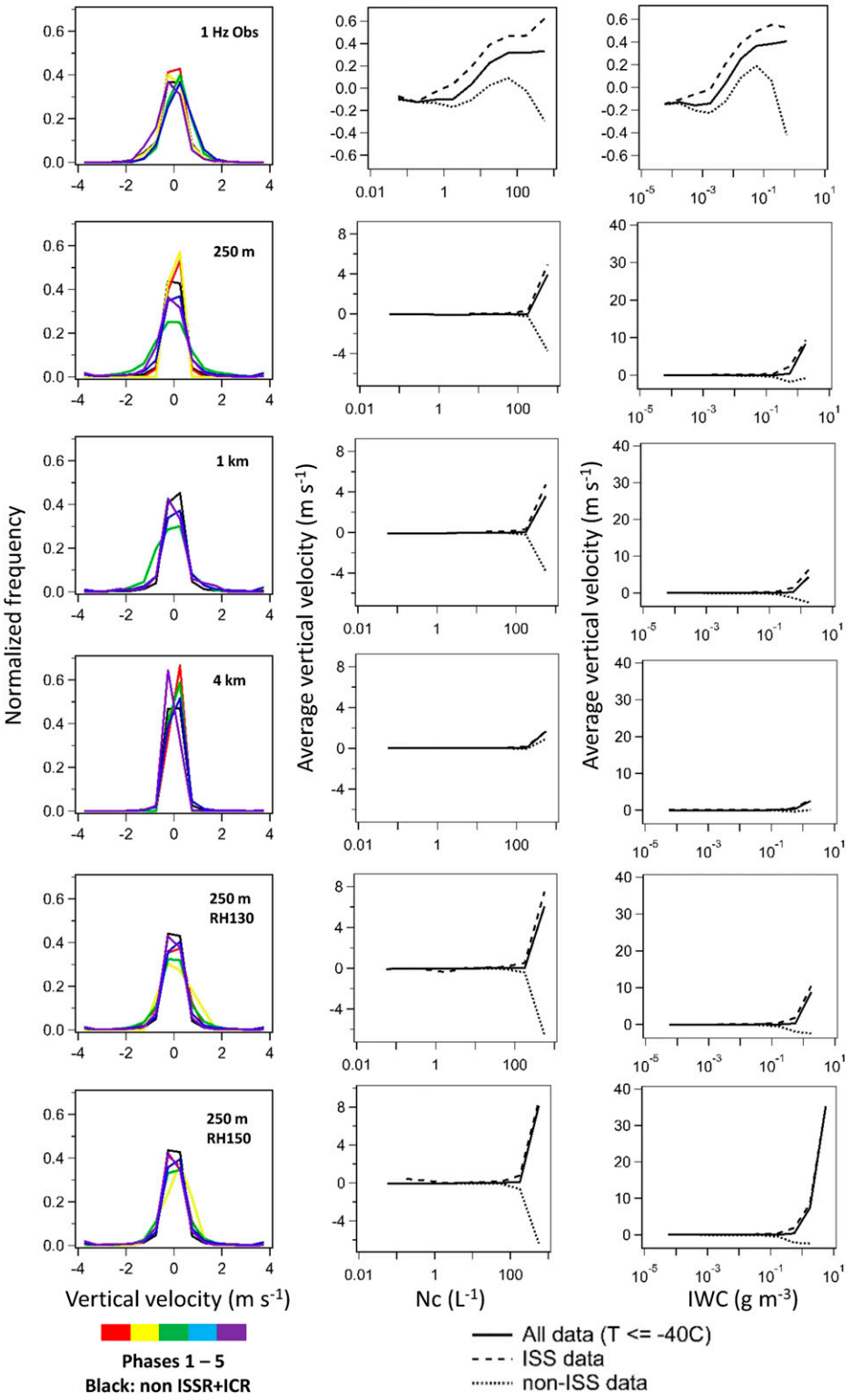

FIG. 15. (left) Normalized frequency distributions of vertical velocity for the five evolution phases of ISSRs and ICRs (binned by 0.5 m s^{-1}). Distributions of the average vertical velocity binned by (center) log-scale Nc and (right) IWC. In the left column, the last bins of vertical velocity are ±4 m s^{-1}, and the values exceeding this range are grouped into the closest last bin.

higher-resolution simulations would be unlikely to produce much more ISS > 8%, as long as the Cooper parameterization has the RHi threshold set at 108%. In fact, Lebo and Morrison (2015) showed that the kinetic energy spectra and the convective core characteristics (in their Figs. 7 and 8) are more similar between 250 m and the higher-resolution simulations (i.e., 100, 66.6, and 33.33 m) than between 250- and 500-m simulations. The small sensitivity of ISS > 8% to the horizontal grid spacing (for $\Delta x < 1$ km) in our study suggests that even though higher-resolution simulations would likely have a less intense updraft and/or downdraft (such as shown in Fig. 15), the direct relationship between the magnitude of ISS and the initiation threshold in the Cooper parameterization would still lead to a sharp decay in ISS frequency when the Cooper parameterization is activated and effectively removes ISS above the threshold.

When examining the sensitivities of the simulated ISSR characteristics to parameters used in the microphysics scheme, the RHi threshold for initiating the Cooper parameterization was found to play a major role. Among several tests, only the simulations with an increased RHi threshold for the Cooper parameterization from 108% to 130% or 150% improved most ISSR characteristics examined in this study, including the magnitude and frequency of ISS, the relationships between RH_{max} (RH_{ave}) and ISSR lengths, and occurrence frequencies of the five evolution phases of ISSR + ICR samples. However, only slight improvements were seen for the horizontal extent of ISSRs, the spatial ratio of ICR/ISSR, and the average IWC during the evolution of ISSRs and ICRs. These improvements were consistent among RH130 runs with 0.25-, 1-, and 4-km horizontal grid spacings (Table 1). Other sensitivity tests (i.e., decreasing the vapor deposition rate, decreasing the IN number concentration in the Cooper parameterization, turning off heterogeneous contact and immersion freezing, or turning off homogeneous freezing of cloud water) did not improve the magnitude and frequency of the higher ISS (i.e., >8%). Furthermore, the RH130 run shows comparable dynamical conditions to the 250-m control simulation, while the RH150 run shows much higher average vertical velocity for ISS with large IWC. Thus, our analysis suggests that the RHi threshold for initiating ice should be set around 130% but below 150% to improve the representation of ISSRs. Such a recommendation is consistent with another study that used real case simulations from the WRF Model, which suggested setting the RHi threshold to be greater than 125% (D'Alessandro et al. 2017).

Cirrus properties have been previously shown to link with MCS evolution. For example, the radiative properties (e.g., heating) of the extended layer of high clouds were shown to play a dominant role in the organization of tropical convection in radiative–convective equilibrium experiments (e.g., Stephens et al. 2008), and the effects of anvil cirrus shading (i.e., attenuation of solar radiation) on buoyancy and updrafts were found to modify the structure and evolution of MCSs (e.g., Oberthaler and Markowski 2013). Given the influence of ISSRs on the formation and evolution of ice crystals, biases in the representations of ISSRs can subsequently influence the simulated cirrus cloud properties, which motivates a focus on improving the simulated ISS and cirrus properties in the context of organized deep convection and squall lines. Since the current study does not include radiative transfer, the impacts of the biases in ISS and ice nucleation parameterizations on MCS structure and evolution could be different when radiation is included. Future investigation is recommended to quantify the impacts of modifying the Cooper parameterization on MCS simulations with radiative transfer calculations, particularly by increasing the RHi threshold.

Acknowledgments. M. Diao acknowledges the support from the National Science Foundation (NSF) Division of Atmospheric and Geospace Sciences (AGS) grant #1642291, and the National Center for Atmospheric Research (NCAR) Advanced Study Program (ASP) postdoctoral fellowship in 2013–15. In addition, she acknowledges the support from the NCAR/ASP Faculty Fellowship and the host of the NCAR Earth Observing Laboratory/Research Aviation Facility for her group in summer 2016. The NSF DC3 campaign dataset is publicly available and can be accessed online (http://data.eol.ucar.edu/master_list/?project=DC3). For the instrumentation field support, calibration, and quality control, the water vapor measurements from the VCSEL hygrometer were supported by J. P. DiGangi, M. Diao, M. Zondlo, and S. Beaton, and the measurements of the Fast-2DC probe received QA/QC support from A. Bansemer. We also acknowledge the support from the flight crew and technicians from the NCAR Research Aviation Facility.

REFERENCES

Adlerman, E. J., and K. K. Droegemeier, 2002: The sensitivity of numerically simulated cyclic mesocyclogenesis to variations in model physical and computational parameters. *Mon. Wea. Rev.*, **130**, 2671–2691, doi:10.1175/1520-0493(2002)130<2671:TSONSC>2.0.CO;2.

Barth, M. C., and Coauthors, 2015: The Deep Convective Clouds and Chemistry (DC3) field campaign. *Bull. Amer. Meteor. Soc.*, **96**, 1281–1309, doi:10.1175/BAMS-D-13-00290.1.

Bryan, G. H., 2005: Spurious convective organization in simulated squall lines owing to moist absolutely unstable layers. *Mon. Wea. Rev.*, **133**, 1978–1997, doi:10.1175/MWR2952.1.

——, 2012: Effects of surface exchange coefficients and turbulence length scales on the intensity and structure of numerically simulated hurricanes. *Mon. Wea. Rev.*, **140**, 1125–1143, doi:10.1175/MWR-D-11-00231.1.

——, and R. Rotunno, 2007: Roll circulations in the convective region of a simulated squall line. *J. Atmos. Sci.*, **64**, 1249–1266, doi:10.1175/JAS3899.1.

——, and ——, 2009a: The influence of near-surface, high-entropy air in hurricane eyes on maximum hurricane intensity. *J. Atmos. Sci.*, **66**, 148–158, doi:10.1175/2008JAS2707.1.

——, and ——, 2009b: The maximum intensity of tropical cyclones in axisymmetric numerical model simulations. *Mon. Wea. Rev.*, **137**, 1770–1789, doi:10.1175/2008MWR2709.1.

——, and M. D. Parker, 2010: Observations of a squall line and its near environment using high-frequency rawinsonde launches during VORTEX2. *Mon. Wea. Rev.*, **138**, 4076–4097, doi:10.1175/2010MWR3359.1.

——, and H. Morrison, 2012: Sensitivity of a simulated squall line to horizontal resolution and parameterization of microphysics. *Mon. Wea. Rev.*, **140**, 202–225, doi:10.1175/MWR-D-11-00046.1.

——, J. C. Wyngaard, and J. M. Fritsch, 2003: Resolution requirements for the simulation of deep moist convection. *Mon. Wea. Rev.*, **131**, 2394–2416, doi:10.1175/1520-0493(2003)131<2394:RRFTSO>2.0.CO;2.

——, J. C. Knievel, and M. D. Parker, 2006: A multimodel assessment of RKW theory's relevance to squall-line characteristics. *Mon. Wea. Rev.*, **134**, 2772–2792, doi:10.1175/MWR3226.1.

Cooper, W. A., 1986: Ice initiation in natural clouds. *Precipitation Enhancement: A Scientific Challenge, Meteor. Monogr.,* No. 43, *Amer. Meteor. Soc.*, 29–32, doi:10.1175/0065-9401-21.43.29.

Cziczo, D. J., and Coauthors, 2013: Clarifying the dominant sources and mechanisms of cirrus cloud formation. *Science*, **340**, 1320–1324, doi:10.1126/science.1234145.

D'Alessandro, J. J., and Coauthors, 2017: Dynamical conditions of ice supersaturation and ice nucleation in convective systems: A comparative analysis between in situ aircraft observations and WRF simulations. *J. Geophys. Res. Atmos.*, **122**, 2844–2866, doi:10.1002/2016JD025994.

Diao, M., L. Jumbam, J. Sheffield, E. F. Wood, and M. A. Zondlo, 2013a: Validation of AIRS/AMSU-A water vapor and temperature data with in situ aircraft observations from the surface to UT/LS from 87°N–67°S. *J. Geophys. Res. Atmos.*, **118**, 6816–6836, doi:10.1002/jgrd.50483.

——, M. A. Zondlo, A. J. Heymsfield, S. P. Beaton, and D. C. Rogers, 2013b: Evolution of ice crystal regions on the microscale based on in situ observations. *Geophys. Res. Lett.*, **40**, 3473–3478, doi:10.1002/grl.50665.

——, ——, ——, L. M. Avallone, M. E. Paige, S. P. Beaton, T. Campos, and D. C. Rogers, 2014a: Cloud-scale ice-supersaturated regions spatially correlate with high water vapor heterogeneities. *Atmos. Chem. Phys.*, **14**, 2639–2656, doi:10.5194/acp-14-2639-2014.

——, ——, ——, and S. P. Beaton, 2014b: Hemispheric comparison of cirrus cloud evolution using in situ measurements in HIAPER Pole-to-Pole Observations. *Geophys. Res. Lett.*, **41**, 4090–4099, doi:10.1002/2014GL059873.

——, J. B. Jensen, L. L. Pan, C. R. Homeyer, S. Honomichl, J. F. Bresch, and A. Bansemer, 2015: Distributions of ice supersaturation and ice crystals from airborne observations in relation to upper tropospheric dynamical boundaries. *J. Geophys. Res. Atmos.*, **120**, 5101–5121, doi:10.1002/2015JD023139.

Ferrier, B. S., W.-K. Tao, and J. Simpson, 1995: A double-moment multiple-phase four-class bulk ice scheme. Part II: Simulations of convective storms in different large-scale environments and comparisons with other bulk parameterizations. *J. Atmos. Sci.*, **52**, 1001–1033, doi:10.1175/1520-0469(1995)052<1001:ADMMPF>2.0.CO;2.

Flatau, P. J., R. L. Walko, and W. R. Cotton, 1992: Polynomial fits to saturation vapor pressure. *J. Appl. Meteor.*, **31**, 1507–1513, doi:10.1175/1520-0450(1992)031<1507:PFTSVP>2.0.CO;2.

Fovell, R. G., and Y. Ogura, 1989: Effect of vertical wind shear on numerically simulated multicell storm structure. *J. Atmos. Sci.*, **46**, 3144–3176, doi:10.1175/1520-0469(1989)046<3144:EOVWSO>2.0.CO;2.

——, and P. S. Dailey, 1995: The temporal behavior of numerically simulated multicell-type storms. Part I. Modes of behavior. *J. Atmos. Sci.*, **52**, 2073–2095, doi:10.1175/1520-0469(1995)052<2073:TTBONS>2.0.CO;2.

——, and P.-H. Tan, 1998: The temporal behavior of numerically simulated multicell-type storms. Part II: The convective cell life cycle and cell regeneration. *Mon. Wea. Rev.*, **126**, 551–577, doi:10.1175/1520-0493(1998)126<0551:TTBONS>2.0.CO;2.

Fusina, F., and P. Spichtinger, 2010: Cirrus clouds triggered by radiation, a multiscale phenomenon. *Atmos. Chem. Phys.*, **10**, 5179–5190, doi:10.5194/acp-10-5179-2010.

Gierens, K., and P. Spichtinger, 2000: On the size distribution of ice-supersaturated regions in the upper troposphere and lowermost stratosphere. *Ann. Geophys.*, **18**, 499–504, doi:10.1007/s00585-000-0499-7.

Hane, C. E., 1973: The squall line thunderstorm: Numerical experimentation. *J. Atmos. Sci.*, **30**, 1672–1690, doi:10.1175/1520-0469(1973)030<1672:TSLTNE>2.0.CO;2.

Heymsfield, A. J., L. M. Miloshevich, C. Twohy, G. Sachse, and S. Oltmans, 1998: Upper-tropospheric relative humidity observations and implications for cirrus ice nucleation. *Geophys. Res. Lett.*, **25**, 1343–1346, doi:10.1029/98GL01089.

James, R. P., J. M. Fritsch, and P. M. Markowski, 2005: Environmental distinctions between cellular and slabular convective lines. *Mon. Wea. Rev.*, **133**, 2669–2691, doi:10.1175/MWR3002.1.

Jensen, E. J., and Coauthors, 2001: Prevalence of ice-supersaturated regions in the upper troposphere: Implications for optically thin ice cloud formation. *J. Geophys. Res.*, **106**, 17 253–17 266, doi:10.1029/2000JD900526.

Johnson, D. E., P. K. Wang, and J. M. Straka, 1993: Numerical simulations of the 2 August 1981 CCOPE supercell storm with and without ice microphysics. *J. Appl. Meteor.*, **32**, 745–759, doi:10.1175/1520-0450(1993)032<0745:NSOTAC>2.0.CO;2.

Kahn, B. H., A. Gettelman, E. J. Fetzer, A. Eldering, and C. K. Liang, 2009: Cloudy and clear-sky relative humidity in the upper troposphere observed by the A-Train. *J. Geophys. Res.*, **114**, D00H02, doi:10.1029/2009JD011738.

Koenig, L. R., and F. W. Murray, 1976: Ice-bearing cumulus cloud evolution: Numerical simulation and general comparison against observations. *J. Appl. Meteor.*, **15**, 747–762, doi:10.1175/1520-0450(1976)015<0747:IBCCEN>2.0.CO;2.

Koop, T., B. Luo, A. Tsias, and T. Peter, 2000: Water activity as the determinant for homogeneous ice nucleation in aqueous solutions. *Nature*, **406**, 611–614, doi:10.1038/35020537.

Krämer, M., and Coauthors, 2009: Ice supersaturations and cirrus cloud crystal numbers. *Atmos. Chem. Phys.*, **9**, 3505–3522, doi:10.5194/acp-9-3505-2009.

Lebo, Z. J., and H. Morrison, 2015: Effects of horizontal and vertical grid spacing on mixing in simulated squall lines and

implications for convective strength and structure. *Mon. Wea. Rev.*, **143**, 4355–4375, doi:10.1175/MWR-D-15-0154.1.

Liu, C., M. W. Moncrieff, and E. J. Zipser, 1997: Dynamical influence of microphysics in tropical squall lines: A numerical study. *Mon. Wea. Rev.*, **125**, 2193–2210, doi:10.1175/1520-0493(1997)125<2193:DIOMIT>2.0.CO;2.

McCumber, M., W.-K. Tao, J. Simpson, R. Penc, and S.-T. Soong, 1991: Comparison of ice-phase microphysical parameterization schemes using numerical simulations of tropical convection. *J. Appl. Meteor.*, **30**, 985–1004, doi:10.1175/1520-0450(1991)030<0985:COIPMP>2.0.CO;2.

Morrison, H., J. A. Curry, M. D. Shupe, and P. Zuidema, 2005: A new double-moment microphysics parameterization for application in cloud and climate models. Part II: Single-column modeling of arctic clouds. *J. Atmos. Sci.*, **62**, 1678–1693, doi:10.1175/JAS3447.1.

——, G. Thompson, and V. Tatarskii, 2009: Impact of cloud microphysics on the development of trailing stratiform precipitation in a simulated squall line: Comparison of one- and two-moment schemes. *Mon. Wea. Rev.*, **137**, 991–1007, doi:10.1175/2008MWR2556.1.

Murphy, D. M., and T. Koop, 2005: Review of the vapour pressures of ice and supercooled water for atmospheric applications. *Quart. J. Roy. Meteor. Soc.*, **131**, 1539–1565, doi:10.1256/qj.04.94.

Oberthaler, A. J., and P. M. Markowski, 2013: A numerical simulation study of the effects of anvil shading on quasi-linear convective systems. *J. Atmos. Sci.*, **70**, 767–793, doi:10.1175/JAS-D-12-0123.1.

Ovarlez, J., J.-F. Gayet, K. Gierens, J. Ström, H. Ovarlez, F. Auriol, R. Busen, and U. Schumann, 2002: Water vapour measurements inside cirrus clouds in Northern and Southern Hemispheres during INCA. *Geophys. Res. Lett.*, **29**, 60-1–60-64, doi:10.1029/2001GL014440.

Parker, M. D., and R. H. Johnson, 2004: Simulated convective lines with leading precipitation. Part I: Governing dynamics. *J. Atmos. Sci.*, **61**, 1637–1655, doi:10.1175/1520-0469(2004)061<1637:SCLWLP>2.0.CO;2.

Phillips, V. T. J., P. J. DeMott, C. Andronache, K. A. Pratt, K. A. Prather, R. Subramanian, and C. Twohy, 2013: Improvements to an empirical parameterization of heterogeneous ice nucleation and its comparison with observations. *J. Atmos. Sci.*, **70**, 378–409, doi:10.1175/JAS-D-12-080.1.

Pruppacher, H. R., and J. D. Klett, 2010: *Microphysics of Clouds and Precipitation.* 2nd ed. Springer, 954 pp.

Robe, F. R., and K. A. Emanuel, 2001: The effect of vertical wind shear on radiative–convective equilibrium states. *J. Atmos. Sci.*, **58**, 1427–1445, doi:10.1175/1520-0469(2001)058<1427:TEOVWS>2.0.CO;2.

Rogers, R. R., and M. K. Yau, 1989: *A Short Course in Cloud Physics.* 3rd ed. Pergamon Press, 150–169 pp.

Rotunno, R., G. H. Bryan, D. S. Nolan, and N. A. Dahl, 2016: Axisymmetric tornado simulations at high Reynolds number. *J. Atmos. Sci.*, **73**, 3843–3854, doi:10.1175/JAS-D-16-0038.1.

Spichtinger, P., K. Gierens, and H. Wernli, 2005: A case study on the formation and evolution of ice supersaturation in the vicinity of a warm conveyor belt's outflow region. *Atmos. Chem. Phys.*, **5**, 973–987, doi:10.5194/acp-5-973-2005.

Stephens, G. L., S. van den Heever, and L. Pakula, 2008: Radiative–convective feedbacks in idealized states of radiative–convective equilibrium. *J. Atmos. Sci.*, **65**, 3899–3916, doi:10.1175/2008JAS2524.1.

Stern, D. P., G. H. Bryan, and S. D. Aberson, 2016: Extreme low-level updrafts and wind speeds measured by dropsondes in tropical cyclones. *Mon. Wea. Rev.*, **144**, 2177–2204, doi:10.1175/MWR-D-15-0313.1.

Straka, J. M., and J. R. Anderson, 1993: Numerical simulations of microburst-producing storms: Some results from storms observed during COHMEX. *J. Atmos. Sci.*, **50**, 1329–1348, doi:10.1175/1520-0469(1993)050<1329:NSOMPS>2.0.CO;2.

Szeto, K. K., and H. R. Cho, 1994: A numerical investigation of squall lines. Part I: The control experiment. *J. Atmos. Sci.*, **51**, 414–424, doi:10.1175/1520-0469(1994)051<0414:ANIOSL>2.0.CO;2.

Tan, X., Y. Huang, M. Diao, A. Bansemer, M. A. Zondlo, J. P. DiGangi, R. Volkamer, and Y. Hu, 2016: An assessment of the radiative effects of ice supersaturation based on in situ observations. *Geophys. Res. Lett.*, **43**, 11 039–11 047, doi:10.1002/2016GL071144.

Thorpe, A. J., M. J. Miller, and M. W. Moncrieff, 1982: Two-dimensional convection in non-constant shear: A model of mid-latitude squall lines. *Quart. J. Roy. Meteor. Soc.*, **108**, 739–762, doi:10.1002/qj.49710845802.

Trier, S., C. Davis, D. Ahijevych, M. Weisman, and G. H. Bryan, 2006: Mechanisms supporting long-lived episodes of propagating nocturnal convection within a 7-day WRF Model simulation. *J. Atmos. Sci.*, **63**, 2437–2461, doi:10.1175/JAS3768.1.

Weisman, M. L., W. C. Skamarock, and J. B. Klemp, 1997: The resolution dependence of explicitly modeled convective systems. *Mon. Wea. Rev.*, **125**, 527–548, doi:10.1175/1520-0493(1997)125<0527:TRDOEM>2.0.CO;2.

Wood, R., and P. R. Field, 2011: The distribution of cloud horizontal sizes. *J. Climate*, **24**, 4800–4816, doi:10.1175/2011JCLI4056.1.

Xu, K.-M., and Coauthors, 2002: An intercomparison of cloud-resolving models with the Atmospheric Radiation Measurement summer 1997 intensive observation period data. *Quart. J. Roy. Meteor. Soc.*, **128**, 593–624, doi:10.1256/003590002321042117.

Zondlo, M. A., M. E. Paige, S. M. Massick, and J. A. Silver, 2010: Vertical cavity laser hygrometer for the National Science Foundation Gulfstream-V aircraft. *J. Geophys. Res.*, **115**, D20309, doi:10.1029/2010JD014445.